

POLITECNICO DI TORINO

Master's Degree in Aerospace Engineering



**Politecnico
di Torino**



TÉCNICO LISBOA



**von KÁRMÁN INSTITUTE
FOR FLUID DYNAMICS**

Master's Degree Thesis

Preliminary study on the effects of environmental conditions on Ionic Propulsion

Supervisors

Prof. Filipe S. CUNHA

Prof. Delphine LABOUREUR

Prof. Dario G. PASTRONE

Candidate

Giacomo G. DE SIO

April 2025

Declaration

I declare that this document is an original work of my own authorship and that it fulfills all the requirements of the Code of Conduct and Good Practices of Politecnico di Torino and the Universidade de Lisboa.

We don't read and write poetry because it's cute.
We read and write poetry because we are members of the human race.
And the human race is filled with passion.
Medicine, law, business, engineering.
These are noble pursuits and necessary to sustain life.
But poetry, beauty, romance, love, these are what we stay alive for.

by Professor Keating

Abstract

Recently, the interest in a new type of propulsion for atmospheric flight has rapidly grown. Based on the acceleration of ionised air through a strong electric field, the ionic air-breathing thruster would bring multiple benefits in both environmental and economic terms. The absence of moving parts, low noise production, and no carbon emissions are just some advantages of this technology. However, the feasibility and application of these non-thermal plasma propulsion systems are still in their infancy, which is why the European IPROP project aims to explore their capabilities and improve their performances.

Few, if any, studies in the literature describe how these thrusters are affected by external environmental conditions, such as temperature and humidity. In this context, the role of the von Karman Institute (VKI) is to study, inside a wind tunnel, how these two variables influence the performances of a prototype ion thruster.

This thesis focuses, at least in the first part, on the study of the characterisation of the flow generated by the Low-speed Open-Loop wind tunnel L-7 at VKI in terms of temperature and humidity uniformity. Four different sensors for measuring the aforementioned variables were analysed to find out their static and dynamic response. These were then used both for a mapping of the temperature and humidity profile of the flow, and for the creation of a feedback control loop with the humidifier capable of supplying steam inside the wind tunnel to try to achieve a uniform and constant humidity profile.

In the second part of the experimental campaign, efforts are dedicated to testing the applicability of the Particle Image Velocimetry (PIV) optical technique in the available facility. This technique was then used to calculate the drag, in absence of plasma, produced by an airfoil placed inside the test section, a crucial aspect in order to derive the actual thrust generated by the ionic air-breathing thruster in the future.

In conclusion, this thesis is only the starting point of a larger project: further experimental testing must be carried out to really get to know how the performances of the thruster are affected by external environmental conditions.

Table of Contents

List of Tables	IV
List of Figures	V
List of Variables	IX
Acronyms	XII
1 Introduction	1
1.1 Concept of ionic thruster	2
1.2 State of the art and future application	4
1.3 IPRON project	9
1.4 Objective of the thesis	9
1.5 Thesis Outline	10
2 Experimental setup	11
2.1 L7 wind tunnel	11
2.2 Temperature module	14
2.3 Humidity module	15
2.4 Test section	16
2.5 Instrumentation	18
2.5.1 Temperature and humidity sensor	18
2.5.2 Pressure sensors	31
2.5.3 PIV setup	32
2.5.4 Parametric PIV study for the current setup	35
2.5.5 PIV image acquisition matrix and post processing parameters	42
3 Inlet flow characterisation	45
3.1 Velocity and turbulence uniformity	45
3.2 Temperature uniformity	47
3.3 Humidity uniformity	49

4	Results	51
4.1	Theoretical background on thrust calculation	51
4.2	Analysis of the current case without plasma creation	55
4.3	Experimental Results	60
4.3.1	Analysis of the results	75
5	Conclusions and perspectives	78
	Bibliography	82

List of Tables

2.1	Sensor characterisation	28
3.1	Mean gradient and variance for every temperature map combination	49
4.1	Drag coefficient for the three cases	76

List of Figures

1.1	Geometry and parameters of an EHD thruster in a multiple units wire-to-airfoil configuration [1]	2
1.2	Schematic diagram of the EHD propulsion principle [9]	3
1.3	A typical lifter design from [5]	5
1.4	Ion-powered airship	8
1.5	Ionic thruster box	8
2.1	L-7 low-speed wind tunnel [27]	12
2.2	L-7 low-speed wind tunnel after modifications [28]	12
2.3	Psychrometric chart: Cold water humidifier [28]	13
2.4	Psychrometric chart: Steam humidifier [28]	13
2.5	Type of humidification [28]	13
2.6	Electrical Resistance	14
2.7	Potentiometer	14
2.8	Steady-state study	15
2.9	Steam sprayer	15
2.10	Carel humidifier <i>UR060HL204</i>	16
2.11	First setup tested to analyse the airfoil drag	17
2.12	Final setup to analyse the airfoil drag	17
2.13	Carel DPDC112000 probe	19
2.14	<i>DHT22 – AM2302</i>	19
2.15	Testo probe	19
2.16	<i>P14</i> sensor	20
2.17	Calibration curve for temperature	21
2.18	Calibration surface for humidity	21
2.19	Calibration residuals	21
2.20	Response time for temperature	22
2.21	<i>DHT-22</i> full test without paper	24
2.22	<i>DHT-22</i> full signal with paper	24
2.23	<i>DHT-22</i> response time	25
2.24	<i>DHT-22</i> recovery time	26

2.25	Carel <i>DPDC112000</i> full signal	26
2.26	Carel <i>DPDC112000</i> response time	27
2.27	Carel <i>DPDC112000</i> recovery time	27
2.28	Full signal for Testo400 probe without paper	28
2.29	Full signal for Testo400 probe with paper	28
2.30	Testo response time	29
2.31	Testo recovery time	29
2.32	Full signal from <i>P14</i> sensor	30
2.33	Response time <i>P14</i>	30
2.34	Recovery time <i>P14</i>	31
2.35	Validyne transducer	31
2.36	Validyne demodulator	31
2.37	Pressure transducer calibration	32
2.38	Camera position	33
2.39	PIV setup [36]	35
2.40	Laser sheet and optics	36
2.41	Convergence analysis using POD filter	39
2.42	Convergence analysis without using POD filter	39
2.43	Particles detected, image 1 of 600	41
2.44	Particles detected, image 467 of 600	41
2.45	Particles detected, image 1 of 600	42
2.46	Particles detected, image 467 of 600	42
3.1	Inlet velocity profile	46
3.2	Inlet turbulence intensity	46
3.3	5 m/s, 0% of power	47
3.4	10 m/s, 0% of power	47
3.5	5 m/s, 60% of power	48
3.6	10 m/s, 60% of power	48
3.7	5 m/s, 90% of power	48
3.8	10 m/s, 90% of power	48
3.9	Humidity map without humidifier	50
3.10	Humidity map with humidifier	50
4.1	Force Balance system experimental setup [44]	51
4.2	Three load cells experimental setup [1]	52
4.3	Control volume used for thrust calculation [18]	53
4.4	Control volume used for thrust calculation [19]	56
4.5	Airfoil tested inside the test section	57
4.6	Arbitrary control volume for x-momentum calculation	58
4.7	Displacement vectors field with a $VDP = 63.9\%$	61

4.8	Velocity magnitude field	62
4.9	Velocity profile downstream	63
4.10	Case 1: Displacement vectors field with a $VDP = 95\%$	64
4.11	Case 1: Magnitude velocity field	65
4.12	Case 1: Downstream velocity profile	65
4.13	Case 1: Histogram of velocities	66
4.14	Case 1: Turbulence intensity	67
4.15	Case 1: Vorticity field	68
4.16	Case 1: Divergence field	69
4.17	Case 2: Displacement vectors field with a $VDP = 96\%$	70
4.18	Case 2: Magnitude velocity field	70
4.19	Case 2: Downstream velocity profile	71
4.20	Case 2: Histogram of velocities	72
4.21	Case 2: Turbulence intensity	73
4.22	Case 2: Vorticity field	73
4.23	Case 2: Divergence field	74
4.24	Case 3: Magnitude velocity field	75
4.25	Case 3: Downstream velocity profile	76

List of variables

Roman symbols

- A_f : frontal area of the thruster $[m^2]$
- A : corona discharge area $[m^2]$
- b airfoil span $[m]$
- c : airfoil chord $[m]$
- C_D : drag coefficient $[-]$
- d : distance between the emitter and collector $[m]$
- D : drag $[N]$
- D_h : hydraulic diameter $[-]$
- E : electric field $\left[\frac{V}{m}\right]$
- f : friction factor $[-]$
- F_{EHD} : force induced by an EHD thruster $[N]$
- F_{visc} : viscous force $[N]$
- g : gravitational acceleration $\left[\frac{m}{s^2}\right]$
- h : test section height $[m]$
- I : current intensity $[A]$
- L duct length $[m]$
- L_c : characteristic length scale $[m]$
- M mach number $[-]$

n : normal unitary vector $[-]$
p : pressure $[Pa]$
q : dynamic pressure $[Pa]$
R : total force of the thruster $[N]$
Re reynold number $[-]$
s : distance between two consecutive collectors $[m]$
S₀ : surface of the control volume $[m^2]$
S_{cross} : cross-section area of the cathode $[m^2]$
t : airfoil thickness $[m]$
T : time $[s]$
u : velocity $[\frac{m}{s}]$
V₀ : corona initiation voltage $[V]$
V_a : Voltage applied between the emitter and collector $[V]$
y output signal $[-]$

Greek symbols

ρ : air density $[\frac{Kg}{m^3}]$
ρ_q : charge density $[\frac{C}{m^3}]$
μ : air dynamic viscosity $[\frac{Ns}{m^2}]$
μ_b : ion mobility $[\frac{m^2}{sV}]$
ε : air permittivity $[\frac{F}{m}]$
ε_s : model blockage interference $[-]$
ε_t : total blockage interference $[-]$
ε_w : wake blockage interference $[-]$
Ω : control volume $[m^3]$
τ : time constant $[s]$

Acronyms

DC : Direct Current

EHD : ElectroHydroDynamic

EME : Electro-Mechanical Efficiency

FFT : Fast Fourier Transform

FOV : Field Of View

GUI : Graphical User Interface

HAPS : High-Altitude Platform Station

NI : National Instruments

PIV : Particle Image Velocimetry

POD : Proper Orthogonal Decomposition

RH : Relative Humidity

ROI : Region Of Interest

SDBD : Single Dielectric Barrier Discharge

TD : Thrust Denisty

TPr : Thrust to Power ratio

UAV : Unmanned Aerial Vehicle

VDP : Validation Detection Probability

VTD : Volumetric Thrust Density

Chapter 1

Introduction

Since the beginning of the aviation era (first crewed heavier-than-air flight, 17th December 1903 by Wright brothers), engines capable of providing thrust have always been characterised by the use of moving, often rotating, parts, which demand large consumption of fossil fuels [1].

Nowadays, aerospace companies, engaged in aircraft development, are obliged to respect environmental constraints and because of this they are oriented towards a more sustainable kind of aviation able to reduce carbon emissions in favor of renewable energies [2].

In this context, there are numerous possible proposals to address the problem, but electric propulsion seems to be one of the best alternatives to conventional engines; although some types of electric motors still have moving parts, they are able to achieve high performance with a low environmental impact [3] [4].

Ionic thrusters fall into the category of electric motors: already widely used for space application, these have not yet been employed for atmospheric flight due to limitations that prevent their application (such as low thrust generation and high energy consumption); however, in the last years, the interest towards ElectroHydroDynamics (EHD) propulsion in this field is rapidly growing [1].

This is mainly due to the multiple benefits that such technology would bring to atmospheric flight in both environmental and economic terms for the aviation sector: first of all, the absence of moving parts in the thrust generation would lead to an improvement in the components operating life that make up the thruster and to a consequent reduction of the maintenance required. Moreover, both noise and air pollution would be minimized: such thrusters, indeed, would turn out to be less noisy due to the absence of moving parts and, since the thrust generation mechanism is powered by electricity alone, they would be more sustainable, completely eliminating carbon emissions and providing that the electricity is given by a green source [1].

Finally, this kind of thruster manages to achieve high levels of efficiency in terms of Thrust-to-Power ratio and further improvements are expected: recent

experiments conducted in laboratory by Masuyama and Barrett [5], in fact, have already shown peak values larger than $100 N/kW$, whilst the value for a typical jet aircraft engine is in the order of $2 N/kW$ and $50 N/kW$ for a modern helicopters rotors [6].

However, the feasibility and application of EHD thruster as a method of propulsion is still in its infancy: a viable and adequate propulsion system must provide sufficient, long-lasting thrust without a strong penalty in terms of weight or aerodynamic drag; this sets limits both on the power requirements (that is Thrust-to-Power ratio) and on the frontal area (that is thrust density) of the EHD thruster [7].

1.1 Concept of ionic thruster

ElectroHydrodynamic propulsion is a method of manipulating and moving fluids without any need for moving surface, which employ only basic electrostatic principles and the acceleration of charged particle within an electric field.

The basic configuration of an EHD propulsive system is known as Thruster Unit (see Figure 1.1), which consists of two asymmetric electrodes, an emitter and a collector (that is airfoil-shaped with chord c and thickness t), separated by a distance called gap (d) and both connected to a high direct current (DC) voltage supply. A further degree of freedom in geometric design implies the use of multiple propulsion units; when two or more thruster units are placed one above the other, they form a Thrust Cell: this layout brings in the spacing (s), another design parameter that defines the distance between two consecutive emitters.

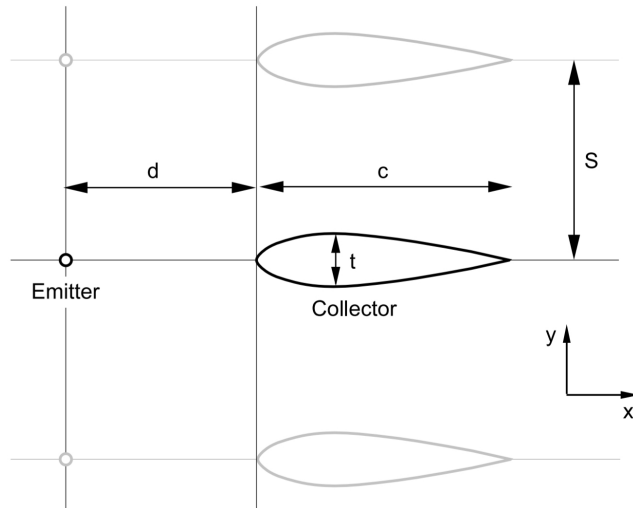


Figure 1.1: Geometry and parameters of an EHD thruster in a multiple units wire-to-airfoil configuration [1]

The presence of a high potential difference among the electrodes allows the so-called Corona Effect to occur: a corona discharge is a self-sustaining atmospheric discharge that is induced by the strong electric field generated between the two conductors and that gives rise to the phenomenon of ionisation of the surrounding air; the ions thus produced are subjected to the electrostatic laws, in particular the Coulomb force, and they are greatly accelerated by the electric field in the so-called drift region from the emitting electrode to the collecting one.

Along this path, the collision with atmosphere's neutral molecules is unavoidable and this allow momentum transfers: the result is a highly accelerated beam of particles, commonly defined as Ionic Wind (Figure 1.2), which, by means of action-reaction principle, generates a net thrust in the opposite direction of ions flow, the so-called ElectroHydroDynamic thrust [8].

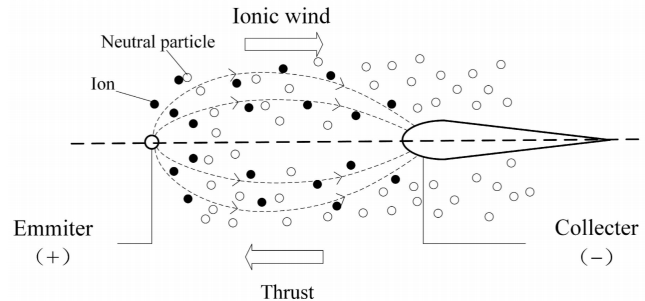


Figure 1.2: Schematic diagram of the EHD propulsion principle [9]

Starting from these basic elements, numerous possible configurations regarding the shape and size of the two electrodes have followed over the years: the emitter, which main purpose is the ionisation of surrounding air, needs to exhibit a very small curvature radius in order to strengthen the local electric field, thus improving ions production; the easiest technology to achieve this is using a metallic wire of radius smaller than $100\mu m$ [10].

Similarly, many studies have been conducted on the collector and the geometry it should assume in order to maximise performance and minimise the aerodynamic drag produced: early configurations used a cylindrical collector, but recent studies have found out that performance was improved by using an airfoil-shaped collector with a conductive surface in the leading edge [7].

Based on this, some performance parameters must be introduced to objectively define the EHD thruster efficiency:

- **Thrust-to-Power ratio (TP_r):** it represents the ratio between the thrust generated by the thruster and the power required by the electrical circuit to produce such a high potential difference between the two electrodes. The

latter is easily obtained from current and voltage measurements within the circuit, whilst for the calculation methodology of the thrust see section 4.1.

As already stated, the results of recent studies on this parameter and its growth expectations represent a key factor in the renewed interest in this new technology.

- **Thrust Density (TD)**: it is defined as the ratio between the generated thrust and the frontal area (spacing, s , multiplied by the spanwise of the airfoil collector, A_f) of the device used; it provides a good relationship between the propulsive force and the thruster size.
- **Volumetric Thrust Density (VTD)**: it plays the same role of the previous parameter but also takes into account the longitudinal length of the collector (the chord, c , if an airfoil-shaped collector is assumed).
- **Electro–Mechanical Efficiency (EME)**: it is defined as the ratio between mechanical and electrical power, it describes the fraction of electrical energy that is converted in mechanical energy.

1.2 State of the art and future application

The most relevant aspect that marks an ionic thruster, as specified in section 1.1, is the possibility of generating net thrust through the acceleration of ions placed between two electrodes by a strong electric field. This phenomenon was first discovered in 1928 by Brown [11][12] and more deeply explored by Christenson and Moller [13] but, despite numerous other studies conducted in the following years, it was concluded that efficiency was greatly reduced by increasing altitude and that some of the performance parameters, such as TPr and the TD , were too low to sustain the flight of a conventional aircraft or any type of application. This led to a gradual loss of interest in the project, which was soon abandoned.

As already mentioned, after an initial stalemate due to technological limitations, interest in EHD thruster has rapidly grown in recent years, especially after studies proved that certain obstacles had now been overcome.

The first devices capable of exploiting EHD propulsion were called "Lifters" [5] [14]: based on a simple triangular structure consisting of a small diameter conductive wire held taut above a vertical aluminium foil, powered by a high voltage among the two electrodes, these devices exploited corona effect to generate an ionic wind and they showed the capability to lift their own weight but not the power source, which is kept on the ground.

The first structure, exploited to provide a physical insight on EHD thruster, involved simple geometries such as wire-to-cylinder configuration: Monrolin, Praud

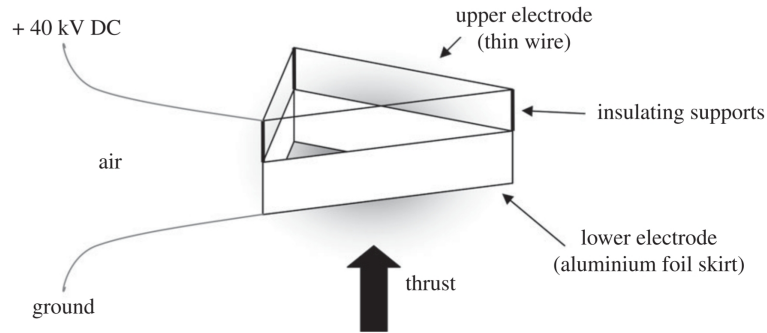


Figure 1.3: A typical lifter design from [5]

and Plouraboué [8] were unable to measure an effective ionic wind between the two electrodes, but they proved that such geometries were strongly subject to drag and that, therefore, aerodynamic effects could not be neglected. This study revealed the importance of the collector's shape in the design of such thrusters.

The following developed flight devices showed to have achieved a much more advanced technological level than the first "Lifters": in particular, Khomich and Rebrov [15] presented a vertical take-off ionocraft powered by a wireless power source, while Xu et al. [7] constructed a light model aircraft capable not only of maintaining stationary flight using EHD thrusters, but also of carrying its own power source. This proved that using this technology with a wire-to-airfoil configuration was capable of powering a small airplane in sustained flight with power supply on board.

From this point on, the wire-to-airfoil configurations have been the subject of numerous studies aiming to explore the capabilities and the possible achievable performance: the first airfoil-shape collector ever investigated in some works was the drop airfoil [16][17], but it was not until 2021 with Belan et al. [18] that a more in-depth analysis of the geometry assumed by the collector was developed.

The latter focused his interest on symmetrical fixed-chord profiles (100mm) in which the maximum thickness and its position were changed, resulting in five different NACA profiles, each organised in a parallel array of thruster units: for each of these, a parametrical study was conducted on the variation of s while keeping emitters and collectors aligned in a 1:1 ratio (one emitter for one collector).

Assuming that if the spacing is too small, performance is worsened due to the shielding phenomenon and that if it is too large, the thruster units act independently of each other, Belan et al. proved that the NACA0010 profile performed best in terms of TPr and TD; they also showed that by increasing spacing, TPr increased to a plateau for all profiles, while TD increased as spacing decreased until an overall maximum was reached.

Finally, a comparison was made between the NACA0010 profile and the drop airfoil: it was shown that the latter performs worse than the former, but is very effective for use in applications requiring high TD .

A year later, further studies by Belan et al. [19] focused on the emitters density (number of emitters in a given length) at a constant gap; in particular, the research involved two different situations, which differed only in their collector spacing: in the first, the thruster cells were composed of NACA0010 profile-shaped collectors spaced 25 mm apart, while the second involved the same collectors spaced 35 mm apart.

The analysis proved that the 2:1 configuration (two emitters per collector) provided the best performance in terms of Thrust density, but the different spacing between emitters did not particularly affect the TPr .

At the same time, the obtained results showed a slight increase in performance for the second configuration, as further proof of the fact that, given the collector shape, a greater distance between collectors was beneficial. Finally, the study also analysed two important cases of electrode positioning in the 1:1 configuration, collinear or staggered alignment: the second geometry showed better performance than the first one only in terms of TPr .

A further parametric research was carried out in 2023 by Kahol, Belan et al. [1] who aimed to analyse different combinations of thickness and chord length for the collector shape, first in a standard configuration ($d = 20mm$, voltage difference applied $V_a = 20kV$, $s = 35mm$ and single emitter), then by varying the spacing between emitters and, lastly, by varying the gap distance and the voltage applied to the electrical circuit.

In the first case, the experiment demonstrated that moving towards shorter and thinner collectors is beneficial, that the family of profile with chord length $c = 25mm$ provided the best performance and, among these, that one which maximised the TPr was characterised by a thickness of $t = 6mm$.

The second case of study has been applied to the aforementioned family and it showed that, for all thicknesses, decreasing spacing resulted in an increase in TD to a local maximum in the single emitter configuration; the same analysis has been developed for the double-emitter configuration revealing that this maximised TPr for high spacing values.

Finally, selected the profile with $c = 25mm$ and $t = 6mm$, it was shown that an increase in the gap, d , led to an increase in performance in terms of TPr , a parameter which, on the other hand, remained constant as the applied voltage varied.

At the end of 2023, Huo et al. [9] developed a UAV powered by six EHD thruster capable, not only flying it, but also enabling the adjustment of the EHD-UAV attitude and flight trajectory through voltage distribution control alone.

Despite all this, no studies are currently available in the literature describing

the behaviour of these air-breathing thrusters under varying external climatic conditions, such as temperature and humidity, as this technology is still in its early stages and under development.

However, numerous studies and devices nowadays use plasma generated through the ionization of the surrounding atmosphere as their main medium. One of the primary examples is the single dielectric barrier discharge (SDBD) actuators, developed for active aerodynamic flow control.

These utilize a physical phenomenon in which an electrical discharge is generated between two electrodes, separated by an insulating dielectric barrier (capable of limiting the discharge and creating a distributed plasma), to generate a net force to the flow.

Numerous studies have been conducted on SDBD actuators and their behaviour under varying external conditions. Although different from the application under examination, these devices operate based on principles very similar to the corona discharge exploited by the ionic thruster and, therefore, represent an excellent starting point for analysing the EHD propulsion system, whose behaviour could be highly comparable.

Regarding humidity variation, in 2012, Bernard et al. [20] demonstrated that, although the SDBD actuator can operate in high-humidity environments (they tested with 98 % relative humidity), the plasma flow velocity generated by the device was highly reduced due to the increase in humidity. In this study, no force developed by the actuator was measured.

Only two years later, in 2014, Ashpis et al. [21] showed, for just two humidity levels, that an increase in relative humidity (RH) resulted in a decrease in the thrust produced by the actuator.

In this context, one of the main studies concerning the effect of relative humidity on the performance of an SDBD actuator was conducted by Wicks and Thomas [22]. They demonstrated, firstly, that no variation in thrust generated by the actuator is observed for $RH < 40\%$, while the thrust tends to decrease with increasing humidity beyond this threshold. This trend is well approximated by a power law, with exponents varying depending on the potential difference between the electrodes and the humidity level reached during the experiment.

Moreover, it was shown that this reduction in the generated force is not due to the decrease in air density caused by increased humidity but rather appears to be associated with the transition in the nature of the discharge, which shifts from a "glow discharge" to a "filamentary discharge" dominated by discrete streamers.

Another aspect pointed out in the latest research concerns the change in plasma chemistry that occurs in a high-humidity environment, the main consequence of which is the increased creation of active species such as OH and H_2O_2 [22]. Greater attention should be given to this topic because the presence of higher or lower humidity can significantly influence the composition of the atmosphere passing

through the thruster and, consequently, the plasma generation.

For example, Kim et al.[23] presented experimental results indicating the importance of oxygen and negative oxygen ions in thrust production by the SDBD actuator.

On the other hand, some studies describe how SDBD actuators respond to changes in temperature. In 2007, Sagawa et al. [24] tested plasma actuators made of alumina ceramic and quartz glass at temperatures up to 600 °C. For a circular configuration actuator, they observed a decrease in performance with increasing temperature, although no force measurements were conducted.

In 2010, however, Vo et al. [25] carried out a quantitative study on the behavior of SDBD actuators, considering not only the temperature around the device but also the external pressure. This research demonstrated an increase in net force produced with rising temperature, in stark contrast to the previous study’s findings (this discrepancy is attributed to the different materials and configurations used).

Furthermore, the study highlighted that an increase in the pressure of the surrounding atmosphere leads to a decrease in the induced velocity and the net force generated, as well as a reduction in plasma density.

As will be further detailed in the following section, one of the main future applications for this new type of propulsion will involve using multiple thrusters to power an airship. The airship could serve as a High Altitude Platform Station (HAPS), namely high-altitude observation missions, which are particularly relevant for both civil and military purposes.

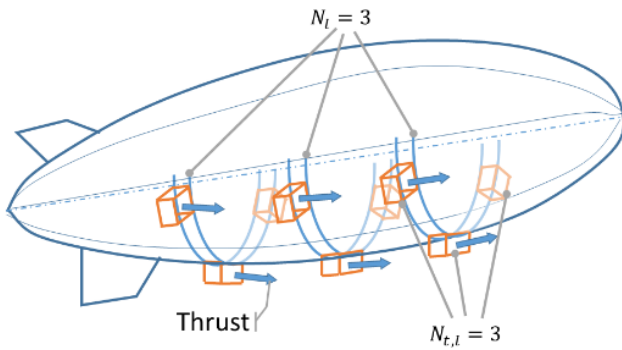


Figure 1.4: Ion-powered airship

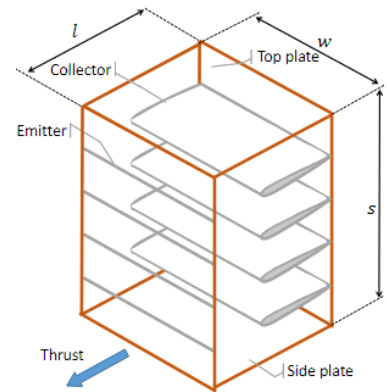


Figure 1.5: Ionic thruster box

1.3 IPROP project

This thesis is part of a wider European project called IPROP (Ionic propulsion for atmosphere), which aims to bring ionic air-breathing propulsive systems beyond the pioneeristic phase, exploring their capabilities and improving their performances [26].

The programme is carried out by several institutions in partnership with each other, including the *Von Karman Institute* (VKI) in Belgium, the *National Centre for Scientific Research* (CNRS) and *Institute Supérieur de l'Aéronautique et de l'Espace* in France, the *Polytechnic of Milano* and the *University of Bologna* in Italy, and the *Technical University of Dresden* and *Karlsruhe Institute of Technology* (KIT) in Germany.

The project, started in November 2023, is still in its infancy and aims, at least in this first phase, to develop an in-depth research into this new technology to be achieved through theoretical, numerical and laboratory studies.

The following steps will lead to develop improved and optimized propulsive units, with the objective of designing and building an airship model (technological demonstrator) with ionic propulsion.

A major long-term impact is expected for ion-powered airships, which could act as stratospheric platforms replacing many satellite functions, such as telecommunications, remote sensing, disaster risk management in civil protection, offering these services at much lower costs, with the benefit of being recoverable systems.

1.4 Objective of the thesis

Many investigations have been conducted to analyse the behaviour of EHD thrusters and to understand how performance parameters are affected, however, as can be seen from section 1.2, these analyses have always focused on geometric optimization of the whole structure by varying spacing, gap and emitter density and on the collector shape by varying chord and thickness.

To date, there are few, if any, studies in the literature that describe how an EHD thruster is affected by external environmental conditions, and this is precisely what the IPROP project aims to focus on at this time.

In this context, the role of VKI is to evaluate how the previously mentioned performance parameters are influenced by the temperature and humidity of the atmosphere surrounding the thruster. To do so, the key idea is to place the latter inside a low-speed open-loop wind tunnel capable of producing specific conditions, offering the possibility of precisely and accurately varying the properties of the incident flow, in terms of speed, temperature and humidity.

This already represents a significant innovation for the project because, at least

up to this point, all the aforementioned researches have studied the the behaviour of the EHD thruster in still air, thus not requiring the presence of an appropriate wind tunnel.

Nevertheless, for the experimental campaign to continue successfully and for the thruster to be placed within the test section, it is necessary that the wind tunnel under consideration has certain properties and meets specific characteristics in terms of flow uniformity inside it.

This thesis, therefore, has as its primary objective the study and the characterisation of this wind tunnel and the testing of certain experimental techniques (such as PIV) to determine whether it can be considered suitable for hosting the thruster.

It is important to emphasise that, after completing my Master's degree, I will continue to work on this project through the Research Master program offered by VKI. Therefore, this thesis should be considered essential for the future continuation of the project.

1.5 Thesis Outline

The thesis is organized as follows: the next chapter, chapter 2, provides a detailed description of the experimental apparatus employed during this study. The first part reviews the facility used, describing the wind tunnel and its characteristics, with particular attention to the temperature and humidity modules. This is followed by a presentation of the sensors used for measurements, along with their respective static and dynamic calibrations. The final part of this section covers the equipment used to implement the PIV technique.

Then, chapter 3 aims to provide an inlet flow characterization in terms of velocity, turbulence intensity, and temperature and humidity uniformity of the flow.

The penultimate chapter, chapter 4, initially presents the methodology used in this setup to calculate the thrust. It then discusses a qualitative parametric study to determine the best configuration for conducting PIV measurements and includes a description of the processing and post-processing of the resulting images. Finally, the last part of this section presents the obtained results.

The final section contains the conclusions drawn from the presented results, along with a final analysis of the work conducted. Particular attention is given to identifying potential improvements to be adopted for future measurements.

Chapter 2

Experimental setup

2.1 L7 wind tunnel

As previously stated, one of this thesis's main purposes is to analyse and understand whether the wind tunnel under consideration could host the ionic thruster and if the generated flow meets specific uniformity characteristics; this implies the necessity of a section describing the initial equipment.

The employed facility is the L-7 open-loop low-speed wind tunnel (see Figure 2.1) provided by VKI's laboratory and it is specially designed to be of economical construction, to require minimal floor space, and to be easily transportable [27].

Capable of achieving a maximum velocity of 20 m/s , the structure framework is made up of six parts: a blower (a centrifugal fan driven by a 700W variable-speed AC motor), a diffuser, which contains two wire meshes and a honeycomb, a horizontal section, that stabilise the flow, a settling chamber, used to reduce turbulence and increase flux uniformity, a $9 : 1$ contraction and, finally, a made-of-plexiglass test section with a cross-sectional area of $20 \times 20\text{ cm}^2$, within the ionic thruster prototype will be placed and location where the flow characterisation will be carried out.

However, due to the need to use a wind tunnel capable of varying temperature and humidity within it, modifications have been made to the L-7 facility: specifically, the horizontal section that separates the diffuser from the settling chamber has been extended to allow for the insertion of the electrical resistance, able to vary the temperature, and multiple sprayers for humidity. The final structure is shown in Figure 2.2.

Furthermore, it's important to highlight and explain the arrangement choice for the components used for flow properties regulation, such as temperature and humidity: in fact from Figure 2.2 it's noticeable that the electrical resistance has been placed upstream of the humidifier sprayers.

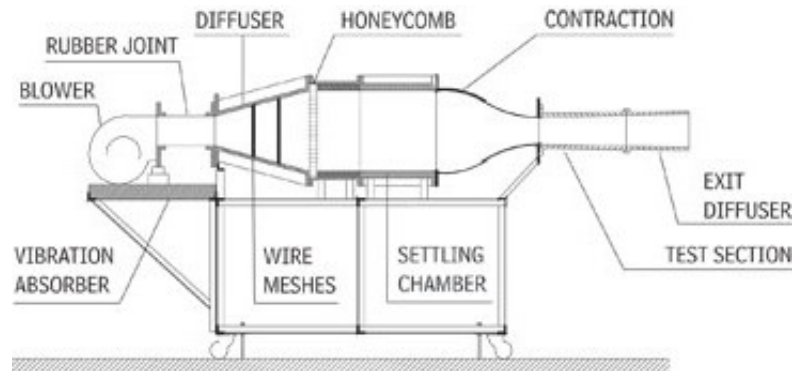


Figure 2.1: L-7 low-speed wind tunnel [27]

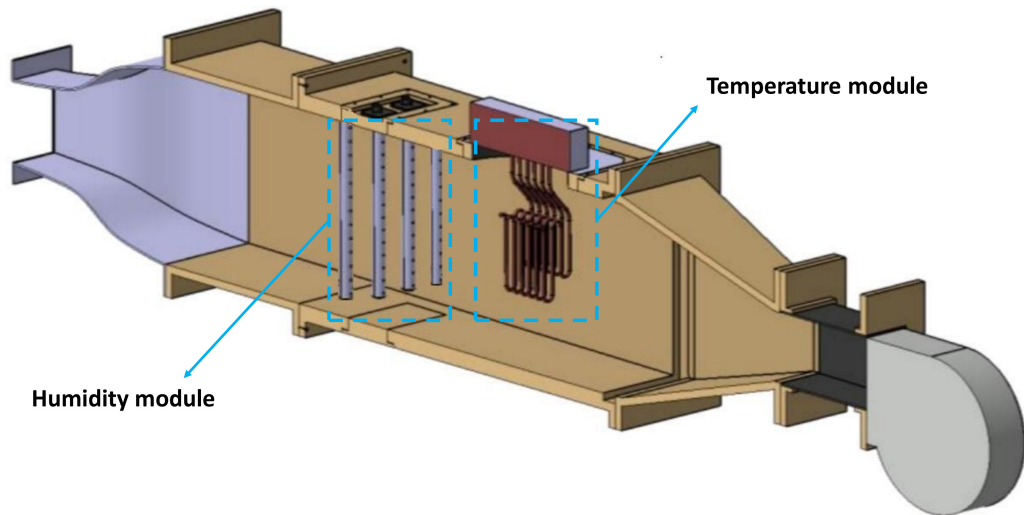


Figure 2.2: L-7 low-speed wind tunnel after modifications [28]

Two possible methods are available for regulating humidity and temperature within the facility: the first uses a type of humidification with cold water and requires both pre-heating and post-heating to reach the desired conditions; the second uses steam humidification and requires only the pre-heating.

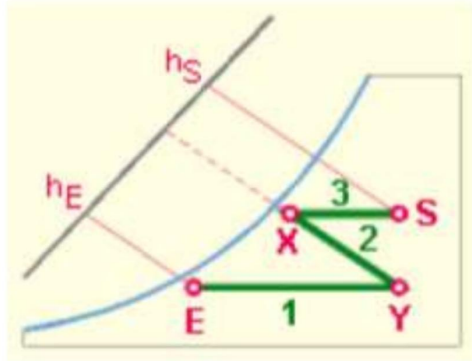


Figure 2.3: Psychrometric chart: Cold water humidifier [28]

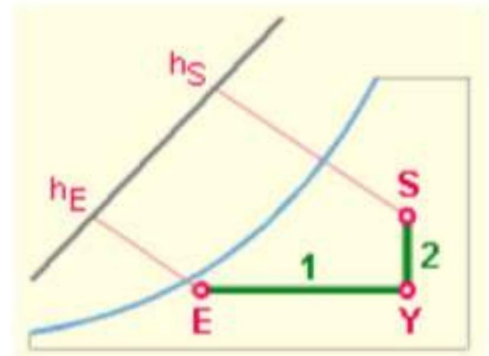


Figure 2.4: Psychrometric chart: Steam humidifier [28]

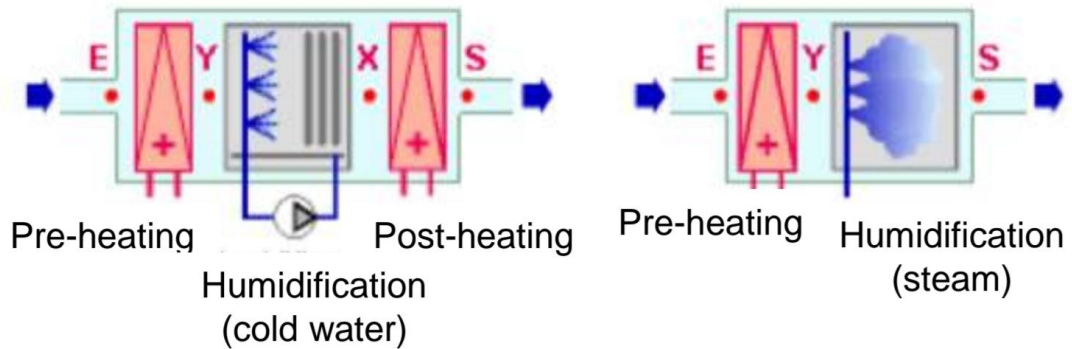


Figure 2.5: Type of humidification [28]

As can be observed by Figure 2.3, Figure 2.4 and Figure 2.5, to get from initial state E to the final S , the first method involves the presence of two intermediate states, Y and X , among which an increase in relative humidity and a decrease in temperature are observed; the temperature must then be restored through the post-heating.

On the other hand, the second method theoretically allows for isothermal humidification of the flow through a single intermediate state Y : the only heating element present is responsible for raising the flow temperature to the desired level without altering the relative humidity, which is subsequently increased by the steam humidifier located downstream.

In practice, although low, an increase in temperature (step 1 E - Y) is associated with a decrease in humidity, and at the same time, the increase in air flow humidity (step 2 Y - S) inevitably causes a temperature variation.

Despite this, the second method appears to be easier to implement, allows for the elimination of the second heating element, and provides the ability to independently control the two flow properties; this explains the choice of positioning the two devices within the wind tunnel.

Given its open-circuit nature, one of the main challenges of the L-7 wind tunnel is achieving a uniform flow in all its properties, a necessary aspect for adequately testing the thruster that will be placed inside the test section. While this does not pose an issue for the velocity field and turbulence intensity of the incoming flow, there are few, if any, examples in the literature of open-loop wind tunnels capable of controlling temperature and humidity to obtain a uniform and consistent profile across the entire test section under examination.

Further details on this will be discussed in the following chapters.

2.2 Temperature module

First of all, it is essential to state that the temperature control inside the chamber is managed by an electrical resistance, designed by the Belgian company Vulcanic, capable of reaching 9 kW of power with a 3×220 V supply. The current supplied by the power source is controlled by an adjustable potentiometer that ranges from 0 to 100%, corresponding to 0 kW (no power) and 9 kW (maximum power) respectively.



Figure 2.6: Electrical Resistance



Figure 2.7: Potentiometer

Flow temperature measurements were carried out using the *Carel DPDC112000* probe at the exit of the test section in twenty different stations (five along the horizontal side \times four along the vertical side), at each of which with the probe acquired data for one consecutive minute and then averaged the results.

A fundamental aspect to understand before carrying out temperature measurements concerns the electric resistance's operation and the time it takes to reach a steady-state operation (time taken to achieve a constant functioning).

Measurement was carried out as follows: the previously calibrated probe was inserted inside the test section, and the blower was simultaneously turned on at a speed of 10 m/s. Subsequently, the electric heater was turned on at 60% of its maximum power, and data acquisition began. Figure 2.8 shows that the time required for the heater to reach a steady-state operation is at least $900\text{ s} / 60 = 15$ minutes. This demonstrates that, before acquiring temperature measurements to build a map of the test section, it is necessary to turn on the resistance and wait for the aforementioned time interval to ensure that the measurements are not biased.

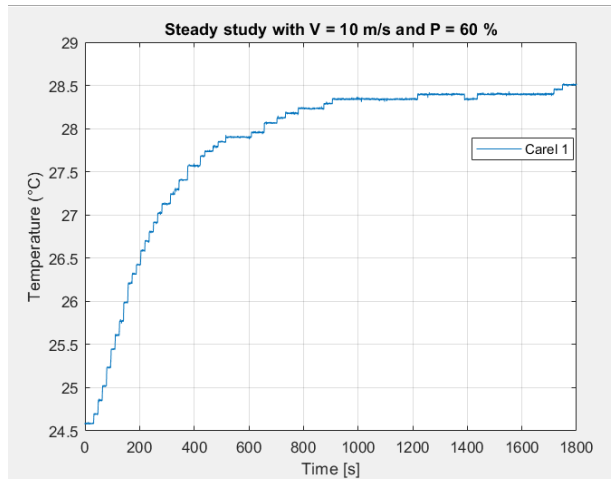


Figure 2.8: Steady-state study

2.3 Humidity module

First of all, it is necessary to state that humidity generation is achieved by an isothermal steam humidifier connected to four sprayers inside the wind tunnel, which are capable of releasing steam (see Figure 2.2 and Figure 2.9).

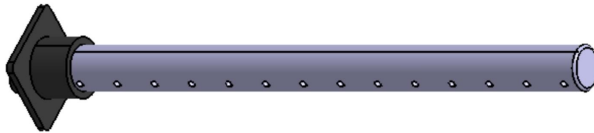


Figure 2.9: Steam sprayer

Designed by the Italian company Carel, the humidifier in question is the *UR060HLL204* model. With this, steam production is controlled with ON/OFF logic or with continuous modulation from 0% to 100% of rated output, using solid state relays (SSR), namely steam production is continuously adjustable based on demand in many different ways: through the use of an external signal, or by means of one or two of the humidity probes and temperature probes.



Figure 2.10: Carel humidifier *UR060HLL204*

The main objective was to generate and maintain a constant and continuous relative humidity within the test section so that, in the future, the EHD ionic thruster could be tested under specific external humidity conditions.

2.4 Test section

As previously mentioned, the test section used is made of plexiglass with a cross-sectional area of $20 \times 20 \text{ cm}^2$, characterized by a length of 1 meter and five pressure tabs evenly spaced along its extension.

This represents the core part of the facility since it is the place where all measurements were carried out: both those related to the static and dynamic characterization of the various sensors (subsection 2.5.1) and those concerning flow uniformity (chapter 3). Moreover, it is within the test section that the NACA 0012 airfoil (with a 0-degree angle of attack) was positioned and subsequently analysed to determine its drag coefficient.

Initially, the setup used for drag calculation included a structure to hold the airfoil in place (shown in Figure 2.11). However, this setup proved to be unusable

due to the significant blockage it created within the test section, strongly affecting the internal flow.



Figure 2.11: First setup tested to analyse the airfoil drag

For this reason, the setup was modified, and the final version involved attaching the airfoil to the test section using two screws, without exploiting an external structure. This solution significantly reduced the blockage effect and allowed for the adjustment of the desired angle of attack (Figure 2.12).

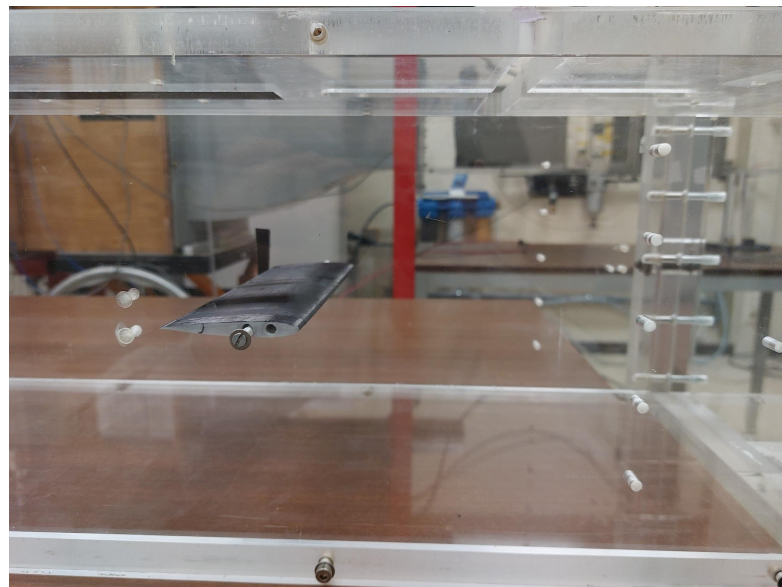


Figure 2.12: Final setup to analyse the airfoil drag

2.5 Instrumentation

Given the experimental nature on which this work is based, it is necessary to provide a detailed description of the instrumentation used to develop it.

This section, therefore, aims to review all the equipment used for the development of this project: first, the temperature and humidity sensors used in the first part of the experiment will be introduced, along with a description of the static and dynamic calibration they required.

Subsequently, pressure sensors will be presented, and finally, a section will be dedicated to describe the instrumentation necessary for applying the optical PIV technique.

2.5.1 Temperature and humidity sensor

As already specified, the main objective of the project is to test the ion thruster under different external conditions within the *L7* low-speed open-loop wind tunnel. However, in order to do this, it is necessary to first develop a characterisation of the inlet flow in terms of temperature and humidity to verify its uniformity and continuity.

Consequently, a series of sensors were used to measure the two quantities mentioned above within the test section.

Description of the different sensors

The first probe to be described is the *CarelDPDC112000* (Figure 2.13): it is a temperature and humidity sensor designed by the Italian company Carel, capable of detecting temperatures between $-10\text{ }^{\circ}\text{C}$ and $60\text{ }^{\circ}\text{C}$ and relative humidity levels between 10 % and 90 %, with analog outputs ranging from 0 – 10 V DC [29].

In this context, it was primarily used for measuring temperature within the test section, as will also be reported in section 3.2.

Another sensor used is the *DHT – 22*, also known as *AM2302* (Figure 2.14). It is a digital device that uses a capacitive humidity sensor and a thermistor to measure temperature and humidity. It communicates using a digital protocol over a single pin, is powered with a voltage of 3 – 5V, and can draw a maximum of 2.5 mA during data conversions.

Despite its low price, theoretically, this sensor appeared to have good response characteristics to humidity variations, being able to sense a temperature range from $-40\text{ }^{\circ}\text{C}$ to $80\text{ }^{\circ}\text{C}$ (resolution $0.1\text{ }^{\circ}\text{C}$) and a humidity range from 0% to 100% (resolution 0.1%) with a sampling frequency of 0.5 Hz [30]. To collect data, the sensor was connected to an *ESP – 32* and a breakout board through a simple Arduino circuit.

Additionally, its size would have allowed for its placement inside the test section without altering the flow or its properties.



Figure 2.13: Carel DPDC112000 probe

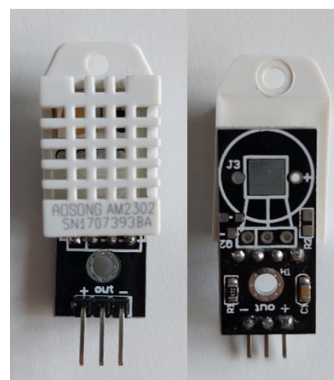


Figure 2.14: *DHT22* – *AM2302*

The third sensor used was manufactured by the German company Testo (Figure 2.15). It allows for the simultaneous measurement of the surrounding environment's temperature, relative humidity, and absolute humidity through a capacitive sensor placed inside it.

This sensor is capable of detecting temperatures between -20°C and 70°C (accuracy of $\pm 0.5^{\circ}\text{C}$, resolution of 0.1°C) and relative humidity levels between 0% and 100% (accuracy of $\pm 2\%$, resolution of 0.1%). This probe transmits data via Bluetooth to the *Testo400*, a multifunctional instrument featuring intelligent calibration, designed by the same company to measure various environmental parameters. For this reason, no calibration was required for this sensor [31].



Figure 2.15: Testo probe

The fourth and last sensor analysed is the Capacitive P 14 Rapid-W (Figure 2.16). Developed by the Swiss company Innovative Sensor Technology, according to its data sheet [32], it features an "ultra fast response time," a "fast recovery time" and it should be "condensation resistant". The technical specifications include operation over a wide temperature range, from -50°C to $+150^{\circ}\text{C}$, and the ability to measure relative humidity from 0% to 100%, with a maximum dew point of $+85^{\circ}\text{C}$. No calibration was necessary because it was provided directly by the company that built it.



Figure 2.16: *P14* sensor

Static calibration

Static calibration takes place under stable and time-invariant conditions. During this procedure, the sensor is exposed to a set of known reference points for temperature and humidity, and its outputs are compared with the standard values. In this case, only the Carel DPDC112000 probe required this type of study.

The calibration of the probe was achieved by placing it inside the *WKL34* climate chamber, capable of creating a temperature and humidity-wise controlled environment, monitoring the output for the entire duration.

The chamber is set to five different relative humidity levels along with 4 different temperatures for each; at every point, the climate chamber is set to spend an hour to ensure that the desired values of temperature and humidity are reached. The obtained data are then used to derive a curve fit that relates temperature to the voltage detected by the probe, and a surface fit to determine the value of relative humidity, using Matlab's Curve Fitting Toolbox (shown in Figure 2.17 and Figure 2.18). The residual related to the calibration surface obtained for the humidity are shown in Figure 2.19.

Dynamic calibration

Dynamic calibration is performed when the sensor is subjected to rapid variations in temperature and humidity. This type of calibration evaluates the sensor's dynamic response to changes, testing its response time and its ability to measure real-time variations in the flow.

As already specified, temperature measurements and the construction of the test section map were carried out exclusively using the *Carel DPDC112000* probe. Therefore, a study was conducted for this probe to evaluate its response time and to understand the time required for the probe to adapt to the flow before starting data acquisition.

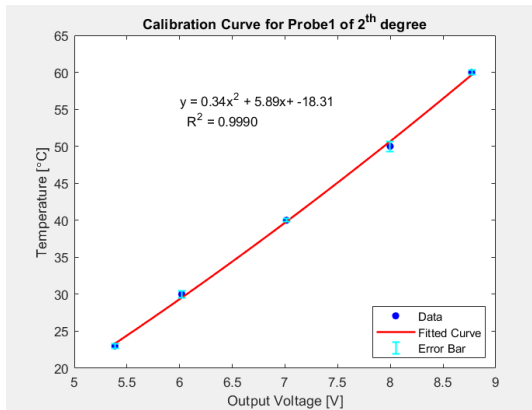


Figure 2.17: Calibration curve for temperature

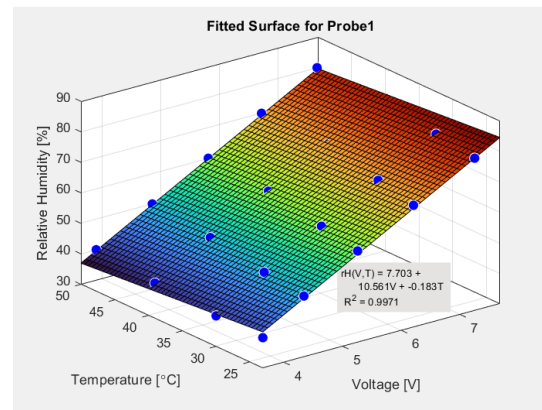


Figure 2.18: Calibration surface for humidity

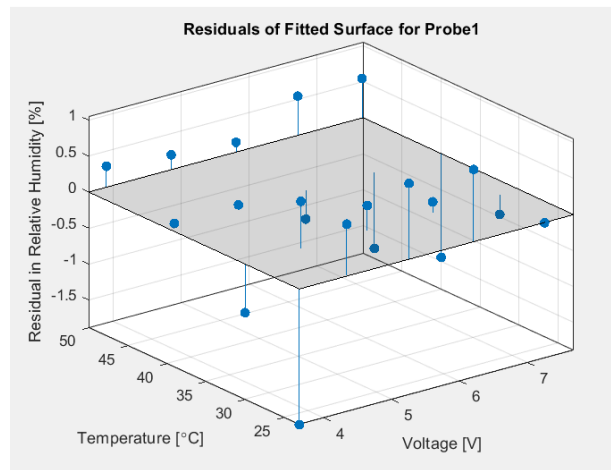


Figure 2.19: Calibration residuals

The study was carried out as follows: a flow speed of 10 m/s and a heater power of 60% of its nominal power were set (same conditions as the steady-state study). Once the heater achieved correct operation, the probe was inserted inside the test section, and data acquisition began.

Figure 2.20 shows an approximate temperature response time of 4 minutes. This implies, as will also be reiterated in section 3.2, that for each measurement station, the probe was inserted into the test section, and only after 4 minutes did data acquisition begin.

On the other hand, regarding humidity, the primary objective was to create an environment with a continuous relative humidity level that was as uniform as possible across the cross-section of the test section. This topic is addressed in

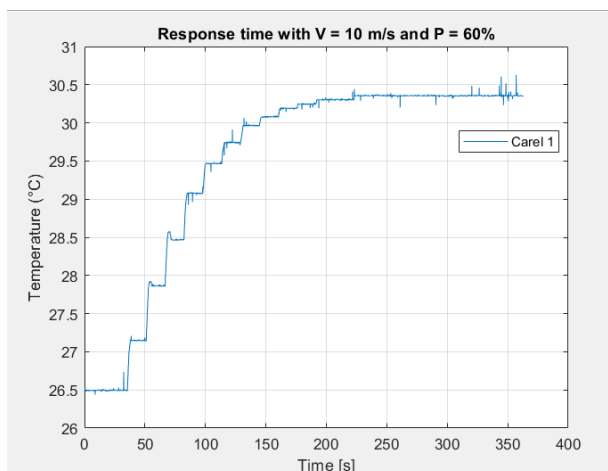


Figure 2.20: Response time for temperature

section 3.3.

Regarding continuity, being one of the few cases in the literature where the goal is to generate constant and controlled humidity within an open-loop wind tunnel, this represented a significant challenge to address.

The initial idea, therefore, was to utilise the feedback control loop mechanism provided by the humidifier by connecting a humidity probe to it, positioned inside the test section.

Right from the beginning, it was clear that the response time of the sensor used played a crucial role in ensuring the proper functioning of the control loop: it was observed that using probes with a slow response time resulted in intermittent puffs of steam from the nozzles, which did not allow for appropriate regulation of the relative humidity in the test section, causing it to fluctuate between excessively high and low values.

It was therefore necessary to conduct a study on the response times of various sensors available, presented above, to determine if any of them were suitable for the required situation. Below are the reviewed probes and their respective characteristics.

Before proceeding, it is necessary to distinguish between response and recovery time, sometimes also referred to as adsorption and desorption response time: the former represents the time the sensor takes to respond to a sudden change in humidity conditions and provide a stable output value (from low to high humidity) in case of adsorption of humidity. The latter, on the other hand, represents the time required for the sensor, in case of desorption of the water vapours, to return to its initial state and be ready to detect a new variation [33].

Usually, the recovery time is longer than the response time, and for this reason,

when choosing the sensor and evaluating its performance, the recovery time must be used as the main evaluation parameter.

Additionally, it is important to highlight that the flow speed passing through the sensor strongly influences the sensor's response and, consequently, its characteristics; in this context, all sensors were analysed under the same flow speed.

Practically, both are commonly defined in the literature as the time required to reach 90% of the variation range and they are strongly influenced by the flow speed they are measuring. Similarly, another key characteristic that distinguishes humidity sensors is the time constant, τ , which is commonly defined as the time the sensor takes to reach 63.2% of its maximum variation [34]. However, since these sensors are first-order systems, they are defined by the canonical differential equation:

$$\tau y' + y = 0$$

where y and y' represent the sensor output and its derivative, respectively. Such systems are characterised by a simple analytical solution describing the exponential decay of the response.

$$y(t) = k e^{-T/\tau}$$

where the constant k is determined by the initial condition and τ represents the characteristic time of the sensor. Consequently, it is possible to fit this equation to the obtained data in order to derive the time constant of the system.

The study was carried out as follows: the sensor was placed inside the test section with a 10m/s flow velocity and with the humidifier turned off for a certain period of time in order to let it achieve the constant, initial value of humidity. Subsequently, the humidifier was turned on at maximum power (due to the inability to regulate it), and finally, it was turned off, and the sensor was left inside the wind tunnel under the influence of the flow to let it return to the initial condition.

It is important to note that turning on the humidifier involves a certain time interval (although small) before it reaches stable operation, and this can be observed from the oscillations present during the increase in humidity in most cases. However, turning it off does not exhibit the same behavior; in fact, the steam stops being produced and released into the chamber a few seconds later without affecting the recovery time.

The first sensor analysed was the *DHT – 22*. This was placed at the test section exit and, following the previously explained procedure, it acquired data for approximately 10 minutes.

From Figure 2.21, it is first possible to notice the presence of oscillations in the initial part of the graph, which, as previously mentioned, represents the time the humidifier takes to reach a steady state.

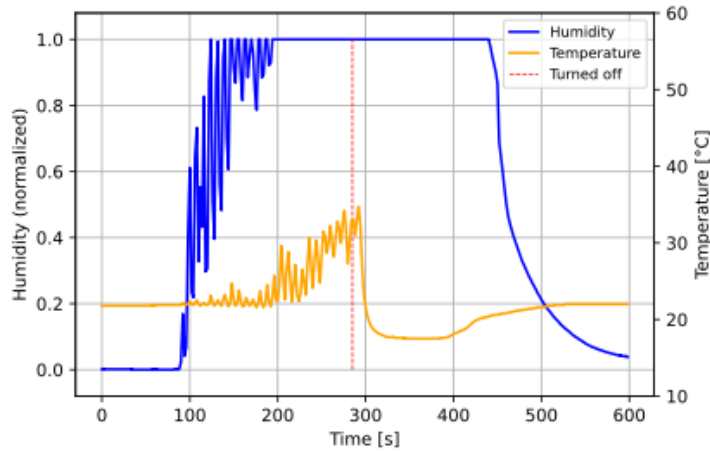


Figure 2.21: *DHT-22* full test without paper

However, what stands out the most is that the sensor continues to detect 100% humidity for more than a minute, despite the humidifier being turned off; this can be attributed to the condensation of water droplets inside the sensor itself, which caused inaccurate readings.

To address this issue, a second measurement was carried out by placing a small piece of paper in front of the sensor; this simple idea significantly improved the sensor's performance characteristics.

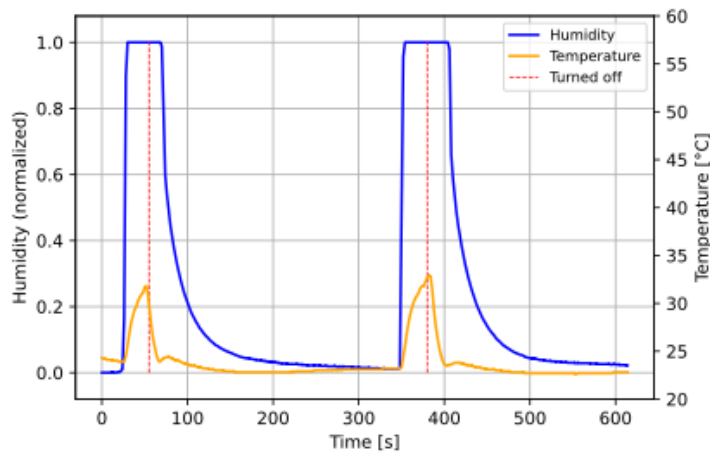


Figure 2.22: *DHT-22* full signal with paper

As can be seen in Figure 2.22, the time during which the sensor detects 100% humidity, after the humidifier is turned off, has decreased to a few seconds, and the recovery time has reduced from around 5 minutes to 2-3 minutes. The detailed

characteristics of the individual sensors analysed are reported in Table 2.1.

Despite this improvement, placing paper in front of the sensor may not be a good long-term solution, as it tends to get wet in high-humidity environments, thereby affecting the measurements.

It would be interesting to find a material that can block the condensation of water droplets inside the sensor, is breathable, and remains unaffected by the presence of humidity.

To analyse the behaviour of the sensor and derive its relevant parameters, the signal chosen was the one from the first activation of the humidifier, specifically the interval between approximately 25 and 340 seconds. Figure 2.23 and Figure 2.24 respectively show the response time and recovery time that characterize the *DHT-22*.

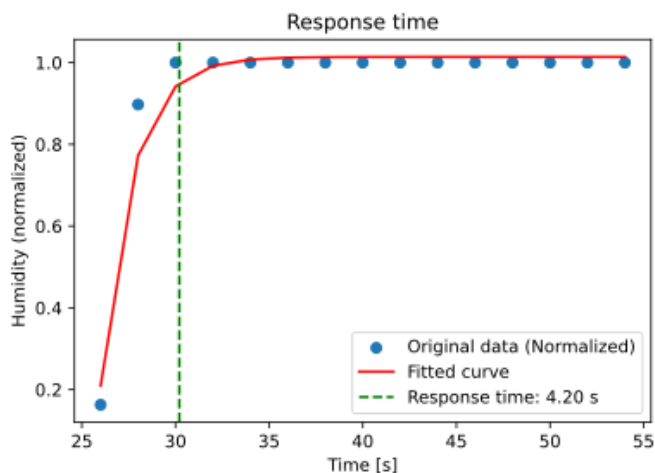


Figure 2.23: *DHT-22* response time

The second sensor studied is the afore-mentioned Carel *DPDC112000*, which provided the result shown in Figure 2.25.

As previously done, it is possible to calculate the parameters characterizing this probe from the complete signal. Figure 2.26 and Figure 2.27 respectively show the response time and recovery time.

Then, the Testo probe was analysed. As with the previous cases, the probe was placed inside the test section, and data was collected for a time interval sufficient to observe both the response time and recovery time (Figure 2.28).

Oscillations can immediately be observed on the left side of the graph, as was the case with both the *DHT-22* sensor and the Carel sensor. These are due to the non-steady-state ejection of vapor by the humidifier’s sprayers.

However, during the execution of these measurements, it was noticed that the condensation phenomenon also strongly affected this probe (though not in the case

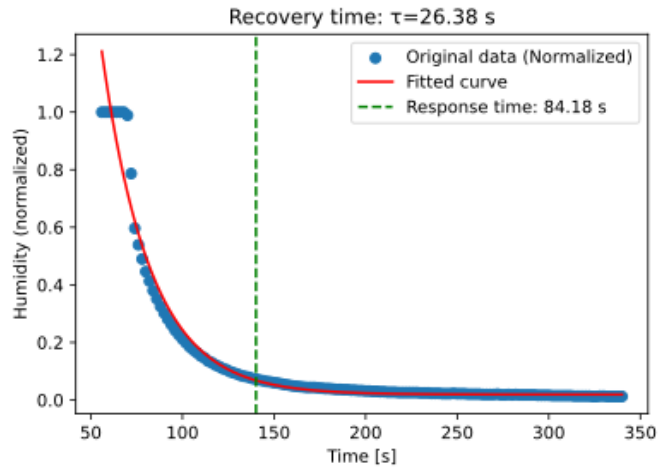


Figure 2.24: *DHT-22* recovery time

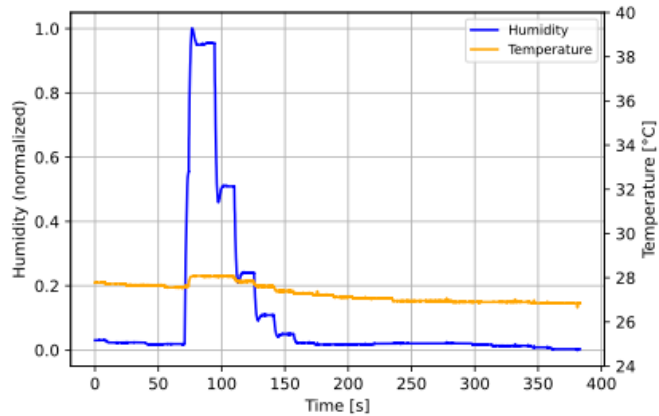


Figure 2.25: Carel *DPDC112000* full signal

just shown). Therefore, a test was conducted using a piece of paper to see if it would improve the sensor’s performance (Figure 2.29).

One of the main aspects observed is that the humidity value detected by the probe does not return to its initial value, indicating that while the paper in front of the sensor solves the condensation issue, it can also influence and distort the perceived humidity readings.

Before moving on to the last sensor, it is possible to analyse the recorded signal in more detail to extract the quantities that characterize the device. Figure 2.30 shows the trend of the response time and its value, while Figure 2.31 displays the recovery time.

The last sensor analysed was the Rapid *P14 – W* over a time period of 30

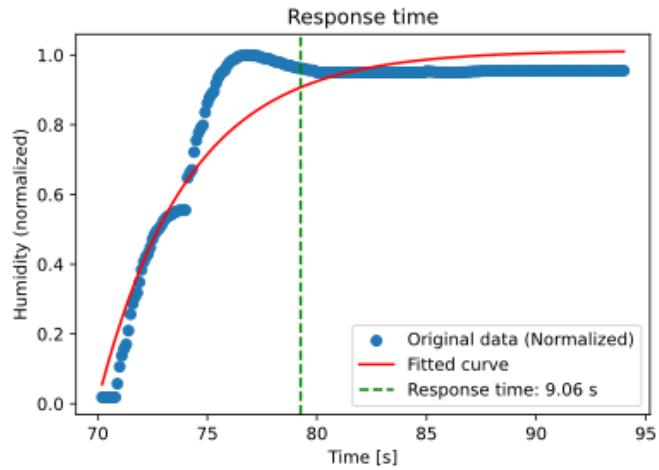


Figure 2.26: Carel *DPDC112000* response time

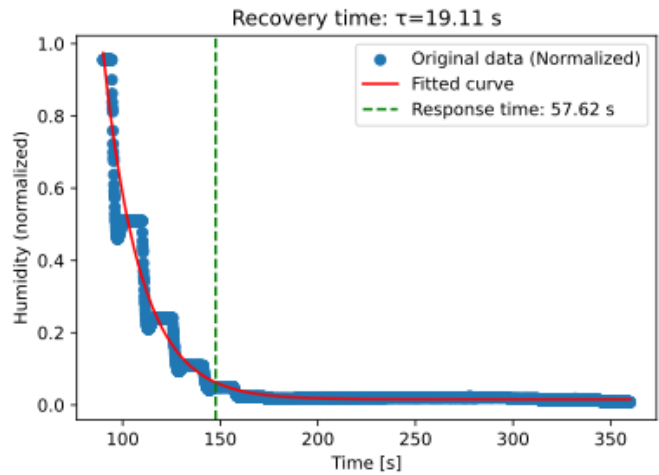


Figure 2.27: Carel *DPDC112000* recovery time

seconds, providing the result shown in Figure 2.32.

Analysing the signal between 11 and 20 seconds, the period during which the humidifier was activated, it is possible to extract the relevant values, namely τ (time constant) from the exponential decay law described above, as well as the response and recovery times based on the previously given definitions. The results obtained are presented in Figure 2.33 and Figure 2.34.

From these graphs, it can be observed that this sensor, as expected, exhibits an extremely rapid response, enabling effective implementation of the feedback control loop via the humidifier. This was impossible to achieve with the other sensors due to their slower response times.

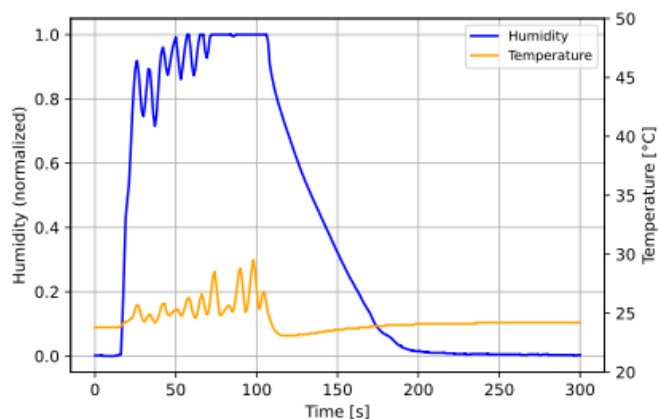


Figure 2.28: Full signal for Testo400 probe without paper

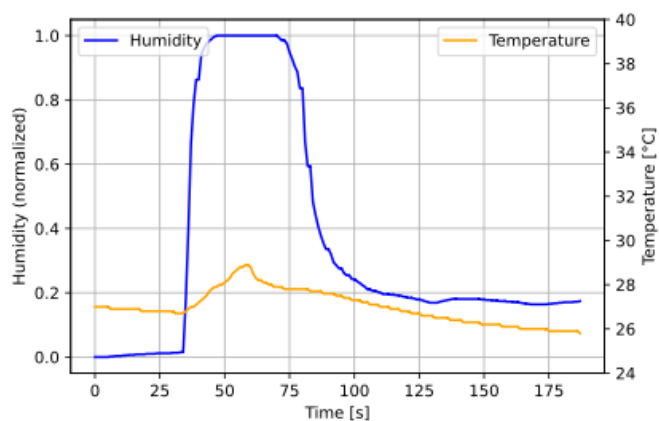


Figure 2.29: Full signal for Testo400 probe with paper

The main characteristics of the analysed sensors are summarized in Table 2.1.

Table 2.1: Sensor characterisation

	DHT-22	Carel	Testo	<i>P14</i>
Time constant τ (s)	26.38	19.11	13.24	0.39
Response time (s)	4.20	9.06	8.44	1.71
Recovery time (s)	84.18	57.62	42.39	1.33

As expected and previously stated, for these types of sensors, the recovery time is usually at least one order of magnitude greater than the response time. This

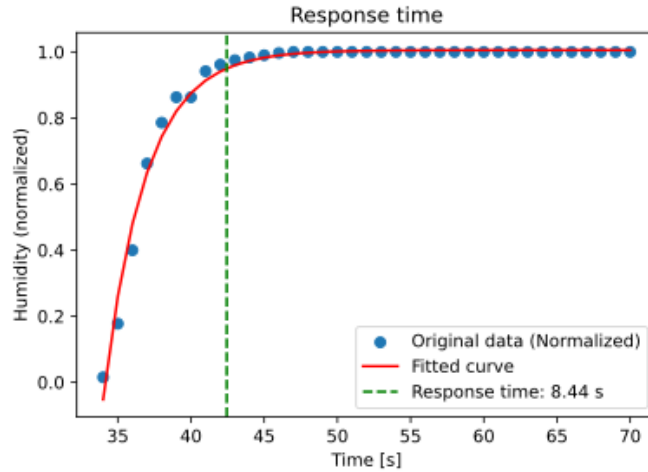


Figure 2.30: Testo response time

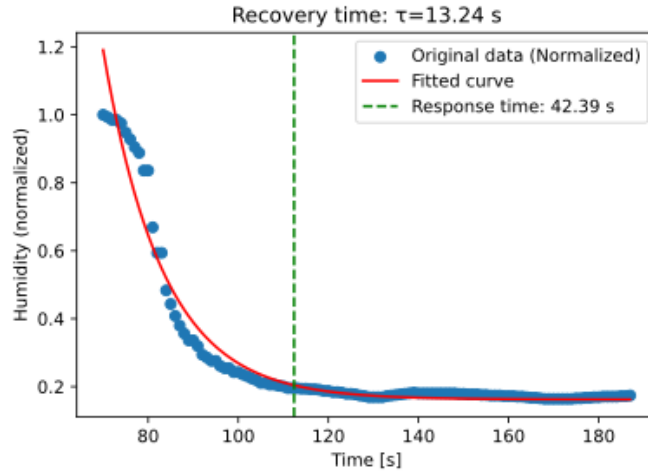


Figure 2.31: Testo recovery time

demonstrates that for dynamic humidity measurements, it is essential to choose a device with the best recovery time.

Another aspect worth pointing out concerns the last sensor, the *P14*. Its performances are significantly better than the other probes tested, with a recovery time that is even shorter than the response time.

Moreover, its small size could allow the installation of multiple *P14* sensors within the test section without significantly altering the flow. This would enable better humidity monitoring, ensuring a flow with both constant and uniform humidity.

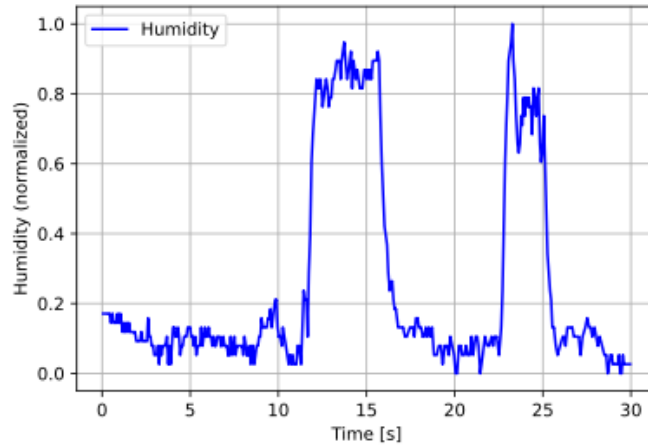


Figure 2.32: Full signal from *P14* sensor

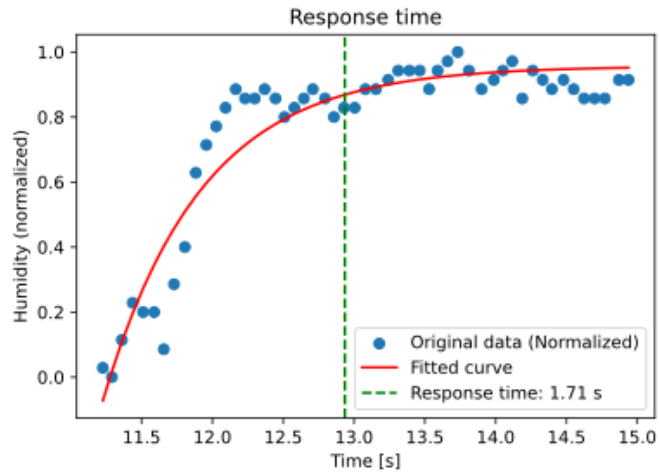


Figure 2.33: Response time *P14*

As can be seen from the Table 2.1, for all four sensors studied, the response time and especially the recovery time are sufficient to allow for the implementation of the feedback control loop provided by the humidifier, but only the last one, the *P14* is precise enough to achieve the desired goal of maintaining a constant humidity within the test section.

However, even in this case, humidity fluctuations were observed, making the control loop mechanism not entirely perfect. To address this issue, the laboratory technicians created a bypass mechanism capable of manually regulating the injection of vapor into the chamber by opening or closing certain valves.

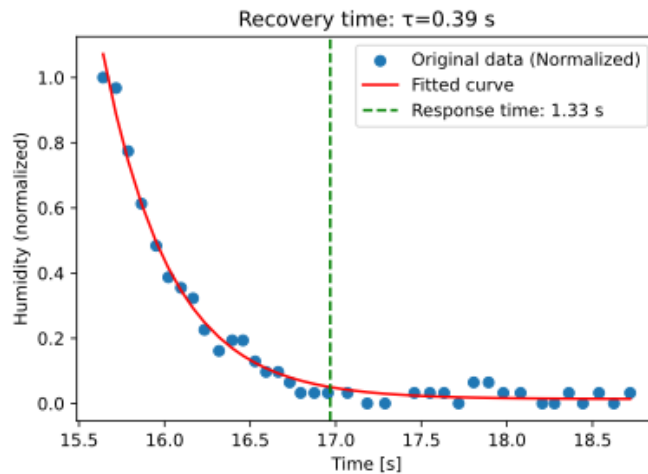


Figure 2.34: Recovery time *P14*

2.5.2 Pressure sensors

During the experiment, pressure measurements were performed using a differential pressure transducer from the Validyne brand (Figure 2.35).

Its operation is based on the principle of magnetic reluctance variation, where a flexible membrane inside the transducer deforms in response to the pressure difference, altering the characteristics of an internal magnetic circuit. This variation is then converted into an electrical signal, which is read and amplified by a carrier demodulator (Figure 2.36), whose role is to demodulate the signal and generate a usable output, typically in voltage or current.



Figure 2.35: Validyne transducer



Figure 2.36: Validyne demodulator

Since it is a highly precise device and strongly affected by external conditions,

regular calibrations were performed each time before its use. In this context, only one example of such calibration is reported (Figure 2.37).

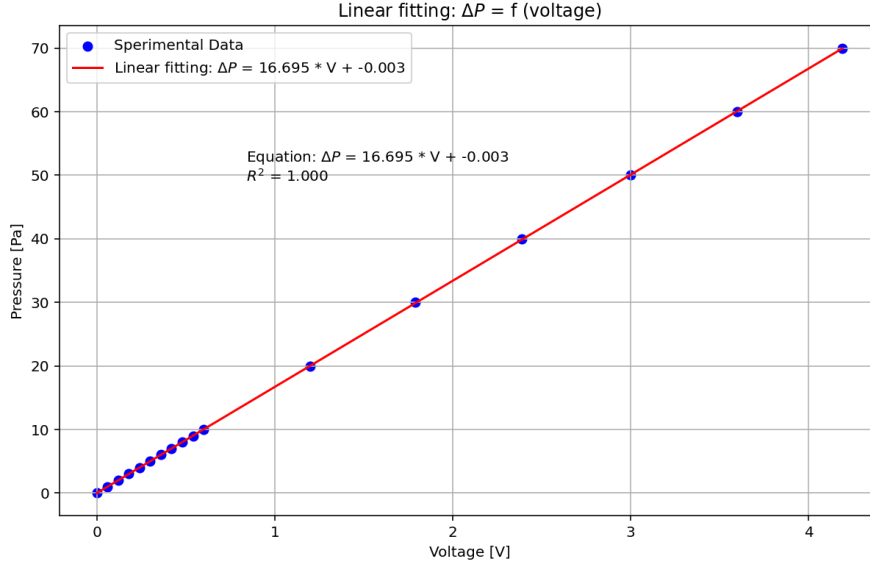


Figure 2.37: Pressure transducer calibration

2.5.3 PIV setup

As will be explained in section 4.2, the methodology for calculating the thrust produced requires knowledge of the velocity profile at the thruster’s inlet and outlet.

Particle Image Velocimetry (PIV) is one of the main optical measurements methods that is employed in literature for flow visualisation and, in this case, it could represent an excellent choice to obtain the desired velocity field.

In this technique, the fluid under examination is seeded with tracer particles which, for sufficiently small size, are assumed to faithfully follow the flow dynamics. By using a laser sheet to illuminate the region of interest and a high-speed camera to capture images, a cross-correlation analysis between successive frames can be developed, allowing the displacement vector of the particles to be obtained. From this, knowing the time elapsed between one frame and the next, it is possible to derive the velocity field of the fluid in the specified region.

In this case, the images were taken using the *La Vision Imager Intense* high-speed camera with variable optics lens based on the field of view of interest, which was connected to a computer and controlled by the *LaVision PIV DaVis* software. The camera was positioned on the left side of the test section (Figure 2.38).

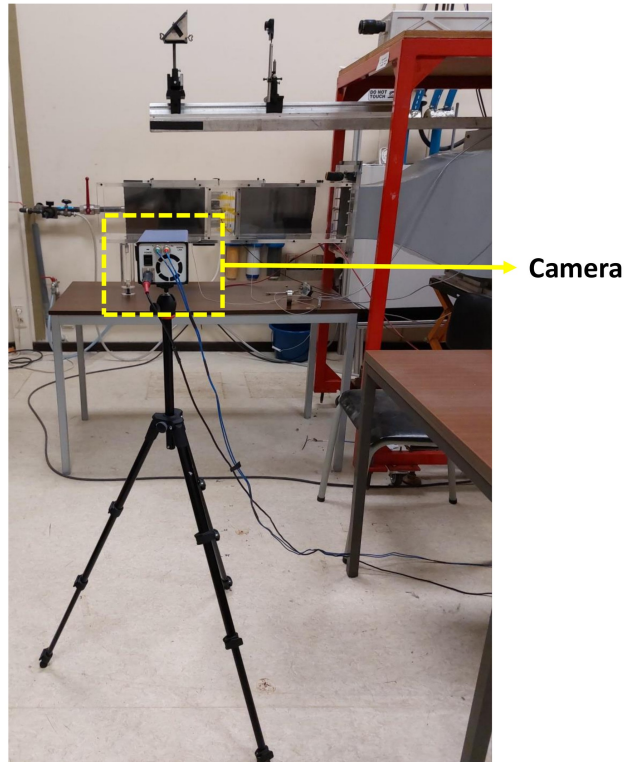


Figure 2.38: Camera position

The positioning and orientation of the camera relative to the test section (inside which the model under study was placed) played a crucial role in the post-processing of the images and in obtaining the desired results.

First of all, the camera must be aligned with the test section to avoid the formation of spurious vectors in the PIV analysis: one of the first studies conducted, indeed, revealed the presence of an anomalous vertical velocity component caused by a slight inclination of the test section (about one degree) that was not considered in the camera's orientation.

Another aspect to consider while placing the camera is certainly the desired velocity profile; the formula Equation 4.5 is based on the application of the momentum conservation equation in two-dimensional form and therefore requires a $2D$ velocity profile. The case under examination used one airfoil, a NACA 0012 profile as a thruster prototype, and it was therefore necessary to position the camera in such a way that it captured only the transverse plane of the profile.

Subsequently, thanks to the use of a dedicated structure, the optics and the laser were mounted above the $L - 7$ wind tunnel in such a way that the laser sheet lay in the flow direction, a crucial aspect for the correct execution of the PIV technique

and to avoid visualising the flow in a plane different from the desired one.

The laser pulse is generated by the Litron NANO L200-15, and to obtain the laser sheet in the desired position and with the correct width, a spherical lens, a cylindrical lens, and a prism were used.

The laser, in turn, was connected to a Programmable Timing Unit (PTU), the hub of all intelligent imaging systems: the latter is responsible for generating precise trigger pulses for cameras, lasers, and other external devices under the control of *DaVis*, ensuring that the timing of the laser pulses and the camera shots are perfectly synchronized. However, as previously stated, in this context, the camera was not directly connected to the PTU but only to the computer, which in turn communicated with the PTU.

Another fundamental aspect to consider in the application of the PIV technique is the choice of particles to be introduced into the flow that the laser will illuminate.

These particles must meet specific requirements in terms of size for the optical method to be appropriately applied. Furthermore, given the future need to implement this technology to study an ion thruster, the main requirement in this situation is that they do not influence the EHD flows. Thus, a key selection must be made regarding the seeding particles, as they might alter the charge distribution in the air and consequently affect performance.

Despite the lack of information regarding PIV implementation in the current design of interest in literature, to find out what kind of seeding particles are used in plasma flows it is possible to analyse the research of Hamdi et al. [35]. The main objective of this research is to propose a method for selecting suitable tracers for PIV measurements in EHD flows. The developed method is based on dimensionless parameters such as the Stokes number (St), which indicates the particle's ability to follow the flow; the Archimedes number (Ar), which quantifies the effects of hydrostatic thrust on the particles; and the electric mobility ratio (M), which measures the influence of the electric field on the particles in relation to the mobility of the fluid. The study examined the following tracer particles: cigarette smoke, incense smoke, SiO_2 micro-balloons, Expancel micro-spheres (EMS), conductive oil smoke, and TiO_2 metallic particles.

Therefore, among the tested tracers, the most suitable for PIV measurements in EHD flows are SiO_2 micro-balloons, TiO_2 particles, and incense smoke, as they follow the fluid flow without being significantly influenced by the electric field. In contrast, tracers such as cigarette smoke and conductive oil particles are unsuitable because they interact too much with the electric field, distorting the measurements.

In conclusion, it was decided to use incense smoke, which was readily available and relatively simple and economic to implement, for the optical PIV technology setup in question. This was placed in a small container positioned above a metal plate at a temperature of $350^\circ C$ inside a seed generation tank. This resulted in the combustion of the incense and the consequent release of particles, which were

pushed into the wind tunnel (specifically in the blower) by means of a gentle flow of air characterised by a variable pressure (between 0 and 2 bar). The choice of the pressure used was made in such a way that a sufficient number of particles within the field of view were visualised based on the case being examined and the velocity of the flow generated by the blower.

The Matlab PIV tool with a graphical user interface (GUI), called PIVlab, was used to analyze the large number of images captured. Its user-friendly interface allows for straightforward image processing, providing the option to apply a mask if necessary, perform pre-processing to eliminate background noise and image contamination, and then apply post-processing after analyzing the frames to remove any outliers present.

The final setup used for the development of the PIV optical technique is schematically shown in Figure 2.39.

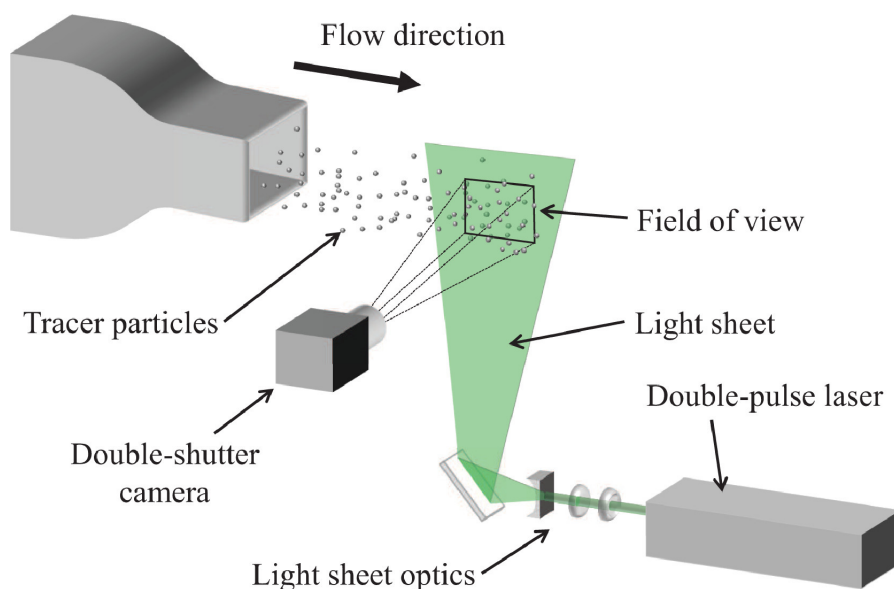


Figure 2.39: PIV setup [36]

2.5.4 Parametric PIV study for the current setup

To properly use the optical PIV technique, it is necessary to perform a parametric study on various factors, often interrelated, that can significantly influence the results obtained with this methodology.

In the current setup, the correct application of this method and the achievement of consistent results, in line with other research, was not immediate: issues arose from time to time that required further analysis and, once resolved, improved the setup and, consequently, the results obtained.

This section, therefore, aims to review the various factors that played a crucial role in the correct execution of the technique [37].

- **Laser**

Together with the camera, the laser plays a key role in this context. Its function is to illuminate the area of interest in the test section, allowing the visualisation of the particles.

One of the main points of concern is certainly its thickness: a laser with excessive thickness risks illuminating particles that are outside the desired measurement plane, i.e., particles that do not belong exactly to the 2D plane intended for analysis.

This introduces information from different depths, leading to results that are not representative of the bidimensional flow and reducing the spatial resolution of the measured profile. Consequently, this can cause errors in calculating the particle displacement and, thus, result in an incorrect velocity field.

To obtain an accurate 2D profile, a thin laser sheet was used to illuminate a specific plane within the flow, minimising the capture of out-of-plane particles. As detailed in Figure 2.39, through the use of a spherical lens, a cylindrical lens, and a prism, along with their respective positioning, it was possible to achieve a laser thickness of approximately 1 mm in the region of interest within the test section (Figure 2.40).

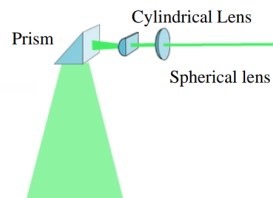


Figure 2.40: Laser sheet and optics

Another aspect concerns the laser intensity chosen to illuminate the seeding particles, whose variation can have different consequences on the quality and accuracy of the measurements.

There is no specific rule of thumb (at least none was found in this context) that defines the required laser intensity: this appears to be strongly related to the camera's aperture. To obtain accurate images, it is necessary to find a combination between these two factors, on a case-by-case basis, that allows for the best possible observation of the particles.

The particles used as tracers must scatter enough light to be detected by the camera; given a fixed aperture, if the laser intensity is not sufficiently high,

the particles may appear too dark or even invisible in the images, making tracking impossible.

On the other hand, an excessively high laser intensity can cause image saturation. This results in a loss of detail, with particles appearing as indistinct white spots, thus preventing accurate motion analysis.

The last aspect to mention concerns the two laser beams generated. In classic PIV applications, such as this one, the velocity field at each time instant is obtained through the cross-correlation of two images (frames) captured almost simultaneously (with a delay on the order of microseconds). To achieve this, the laser generates two separate pulses that illuminate the two different images: initially, the two pulses were slightly misaligned, resulting in a different distribution of illumination between the two images. Once this was identified, the laser was replaced, and the issue was partially resolved.

- **Optics alignment**

The alignment of the laser with respect to the lenses is crucial for obtaining a well-defined optical beam and ensuring that the illumination plane is uniform and has the correct shape.

Initially, the thickness of the laser sheet illuminating the test section was not constant along its length. It was necessary to adjust the positioning of the lenses so that the laser hit the center of each lens perfectly, thereby avoiding any optical phenomena that could distort the beam profile. This was easily accomplished by using several pieces of paper cut to the same shape as the lens in question, which were temporarily attached to the lens itself to check the position of the laser beam.

Additionally, attention had to be paid to the orientation of the prism to ensure that the beam was perpendicular to the test section and parallel to the two side walls.

- **Camera**

As previously mentioned, a fundamental parameter is the camera, whose configuration in a PIV setup is a critical element that significantly affects the accuracy and resolution of the measurements.

One of the most important factors is the distance from the test section at which the camera is positioned. This distance must be chosen based on the required field of view, the desired spatial resolution, and the focal length of the lens used.

With the latter characteristic fixed, the closer the camera is to the test section, the smaller the field of view (FOV) and the higher the spatial resolution

(pixels/mm); conversely, the farther the camera is from the test section, the larger the field of view, which leads to a decrease in spatial resolution.

At the same time, with the camera's distance from the test section fixed, the greater the focal length of the lens used, the narrower the area captured by the lens and the higher the spatial resolution. Conversely, a short focal length provides a wider field of view, resulting in a reduction of spatial resolution.

Usually, the spatial resolution depends on several factors, such as the focal length of the lens used, the distance between the camera and the test section, or the resolution of the camera itself. A good spatial resolution for this setup and application, that provided acceptable results, has been estimated to be between 5 and 7 pxl/mm, and the remaining three parameters were adjusted accordingly based on the case of interest. The choice of this resolution will be further clarified in the subsection 2.5.5, where the method used for the analysis of the obtained frames will be explained in detail.

As previously stated, the choice of the diaphragm aperture was made in relation to the laser intensity used, and a combination of the two was always sought to allow for the best possible visualisation of the particles.

Regarding the camera focus, it must be adjusted precisely to ensure that the particles in the laser plane are well-defined and contrasted. The focus should be optimized on the laser cutting plane, avoiding any out-of-plane particles (in the foreground or background) from affecting the quality of the images. To achieve this, a calibration target made up of numerous small black circles was used, positioned on the laser plane, and the focus was set on it.

- **Convergence analysis**

This involves verifying that the obtained results are reliable and independent of the settings used.

In this context, the number of images taken for a certain case was chosen as a reference parameter to determine the minimum amount of data needed to obtain accurate and stable measurements. The goal was to understand after how many images the velocity value at a specific point in the field of view would converge.

To ensure that this analysis was not influenced by the wake of the airfoil or the airfoil itself, a point was chosen above it at a distance of 1.5 times its chord length, which, theoretically, should have had a constant velocity equal to that of the inlet.

From the Figure 2.41, it can be observed that a good degree of convergence, at least in this case, is achieved after just 200 images: the first four significant digits ($v = 10.73 \text{ m/s}$) remain unchanged as the number of images increases.

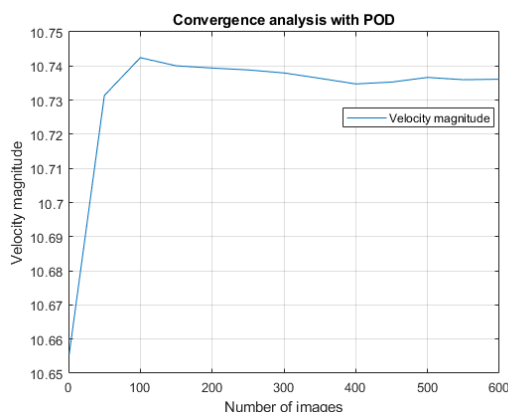


Figure 2.41: Convergence analysis using POD filter

However, the degree of accuracy continues to improve after 500 images, where the significant digits that remain unchanged rise to five ($v = 10.736 \text{ m/s}$).

A notable aspect that needs to be highlighted is the influence that pre-processing applied to the images before analysis has on the convergence of the data.

The Figure 2.41, as indicated by the title, was obtained by applying the Proper Orthogonal Decomposition (POD) filter as pre-processing, a background removal method that will be thoroughly described in the subsection 2.5.5.

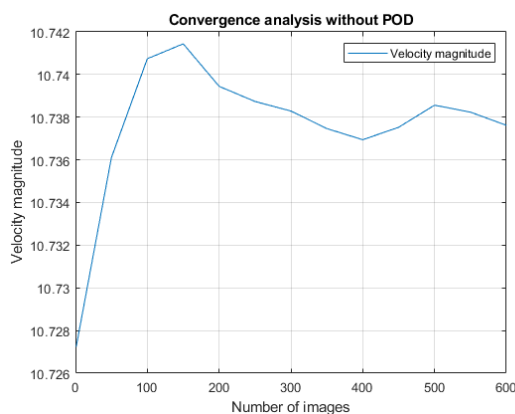


Figure 2.42: Convergence analysis without using POD filter

The Figure 2.42, on the other hand, presents the convergence analysis applied to the same case (and thus the same images) but using the background removal method provided by the Matlab tool PIVlab, which simply subtracts the average intensity from each image.

From this, it can be observed that a good degree of convergence with at least four unchanged significant digits is not achieved after 200 images, nor is it obtained even after 600 images. This demonstrates that the choice of pre-processing method is fundamental for obtaining accurate and consistent results with a not excessively high number of images.

Therefore, for all subsequent analyses, the POD filter was chosen as the pre-processing method, capable of providing a good level of accuracy even after a few images. Additionally, to ensure an adequate degree of convergence, all cases were analysed by acquiring at least 600 images each.

- **Seeding particles**

Since the tracer particles are used to visualize and track the movement of the airflow, it is important that they have a homogeneous distribution at least within the measurement window illuminated by the laser. Furthermore, it is necessary for the concentration to be sufficiently high to ensure a good signal in the camera's field of view.

The mechanism for introducing incense smoke into the wind tunnel can be regulated by two factors: first, it is possible to send pressurized air into the tank to facilitate the passage of particles into the wind tunnel. Second, the airflow generated by the rotation of the blower creates a pressure difference between the tank and the wind tunnel. Therefore, even without directly applying pressure inside the seeding generation chamber, the blower's movement creates a suction effect that draws the seeding into the wind tunnel flow.

Initially, to achieve a high concentration of particles, the container with the incense was left to burn inside the tank for a certain period to accumulate a large amount of smoke. Subsequently, to send these particles into the wind tunnel, pressurised air at about 2 bar was introduced into the tank.

However, this method has a significant drawback: acquiring 600 images takes between 2 and 3 minutes, and it would be ideal to have uniform seeding with an adequate concentration throughout the entire duration of the acquisition.

In this way, however, the introduction of pressurised air into the tank led to a rapid expulsion of the accumulated smoke into the wind tunnel. The result was that a high concentration of seeding characterised the initial images, while the later images showed a much lower concentration, equal to the smoke production rate in the tank, as can be seen in the Figure 2.43 and Figure 2.44.

This, as can be inferred, can strongly influence the analysis performed on the images: the initial ones would indeed be rich in information and thus characterised by a higher resolution. The later images, on the other hand,

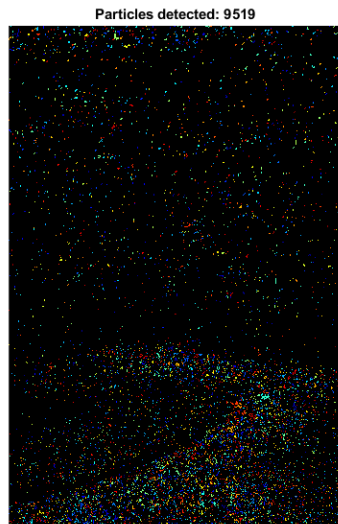


Figure 2.43: Particles detected, image 1 of 600



Figure 2.44: Particles detected, image 467 of 600

having a lower concentration of particles, would be characterised by a lower resolution that could compromise the convergence of the results. The high concentration present in the first frames might lead the analysis to converge quickly and with few images; however, this would then be compromised by the remaining frames that contain less information.

This leads to the conclusion that using pressurised air to introduce incense smoke particles into the wind tunnel is not advisable.

Based on the above, it was decided to avoid using pressure in favour of relying solely on the suction mechanism of the blower. Now, what rotation speed should the blower (and thus the airflow) have in order to achieve uniform seeding with a good concentration throughout the entire duration of the acquisition?

No general rule has been found for this, but theoretically, increasing the rotation speed of the fan results in an increased pressure difference between the tank and the wind tunnel, leading to a stronger suction force.

However, it has been observed that using a lower rotation speed ($1 - 7 \text{ m/s}$) allows for more efficient management of the seeding, resulting in a more or less uniform concentration of particles throughout the entire duration of the acquisition (Figure 2.45 and Figure 2.46).

In general, a PIV analysis can also be conducted at higher flow velocities,



Figure 2.45: Particles detected, image 1 of 600

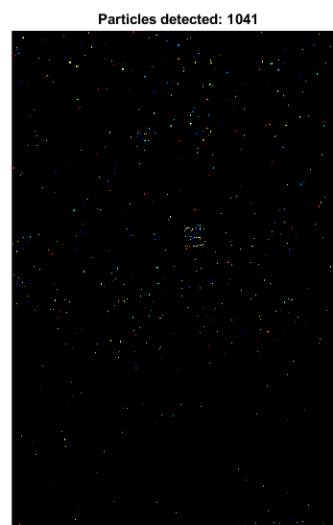


Figure 2.46: Particles detected, image 467 of 600

but different seeding control techniques must be used. Among these, one could consider placing two incense containers inside the tank instead of one to increase the particle generation rate and ensure a higher number of particles throughout the acquisition process.

However, it is important to emphasize that the future study of the plasma thruster, at least in its initial phases, cannot be carried out at high airflow velocities. This is because the higher the flow velocity, the more difficult it will be to detect the presence of the plasma flow generated by the thruster itself [38]. Consequently, a velocity range between 1 and 7 m/s is more than sufficient for the future goals of the project.

2.5.5 PIV image acquisition matrix and post processing parameters

This section aims to provide an accurate description of how the analysis of the acquired images was conducted: the type of pre-processing applied, the parameters set, the post-processing used, and all the steps carried out to obtain a correct examination of the frames.

As already stated in Figure 2.39, image analysis was carried out using the PIVlab tool offered by Matlab, due to the simplicity of its interface and the variety of settings that can be used. This allows, first of all, the definition of a region of

interest (ROI) and enables the application of a mask to exclude certain regions of the image within the ROI from the analysis.

It is important to remark that the accuracy of PIV relies on the quality of the image which constitutes the measurement input signal: under ideal conditions, PIV images should be characterised by a large amount of bright particles with a diameter of 2-3 pixels onto a dark background [39] [40].

In real conditions, however, images are usually affected by a number of background noise sources (such as laser light reflections, light scattering between particles, and random noises) which pollute the correlation map between two consecutive frames.

The background noise reduces the particle contrast and yields spurious correlation peaks, that can sometimes result in spurious displacement estimates if the correlation of the background is stronger than the correlation of the desired signal, thus providing erroneous results not in line with the real experiment.

For this reason, applying pre-processing to the images before the cross-correlation is essential to obtain an analysis that is consistent with the experiment and provides meaningful results.

The GUI-based open-source tool (PIVlab) offers this capability directly on the platform by providing numerous pre-processing techniques.

Among these, two were used most frequently in this analysis: a high-pass filter, which mainly preserves high-frequency information from the particle illumination, suppressing the low-frequency components in the images, and Background Subtraction, which is capable of calculating the mean intensity of a set of input images and subtracting the resulting image from each input image [41] [42].

However, as demonstrated in subsection 2.5.4, the use of pre-processing techniques offered by PIVlab does not allow, at least in the analysed case, the achievement of velocity convergence, a requirement that is instead met by applying the POD filter.

The POD-based background removal [43] is an innovative method for removing background noise in PIV images using Proper Orthogonal Decomposition.

This technique allows the decomposition of a data series (the PIV images) into a set of orthogonal functions (modes) through model order reduction (MOR), which approximates the background noise source and the PIV particle pattern; this filter then automatically identifies and removes the modes representing the background noise.

The strength of this filter lies in the fact that it is insensitive to the size, intensity, and fluctuations of the background noise across different images while maintaining a computational cost comparable to other pre-processing techniques.

In PIV, the velocity field is determined by comparing pairs of images acquired in rapid succession. Image processing was carried out using the Fast Fourier Transform (FFT) window deformation correlation technique. This method first

divides the image into small interrogation windows capable of deforming, which are then examined by the cross-correlation to track the movement of the particles. The Fourier transform is applied to convert the image from a physical space (image space) to a frequency space, where repetitive patterns in the movement of particles can be identified, making the motion estimation process more robust and less sensitive to changes not related to the flow [41] [42].

PIVLab allows for the execution of an iterative process that performs three successive passes with progressive reductions in the interrogation window size and window deformation to improve spatial resolution. In each pass, the velocity field estimated in the previous step is used to deform the interrogation windows for the next pass.

In this analysis, three passes were used: the first employed a large interrogation window ($128 \times 128 \text{ pixel}$) to obtain an initial velocity estimate characterized by low spatial resolution. Then, a smaller window ($64 \times 64 \text{ pixel}$) with deformation was used to better adapt to local velocity variations in the flow. Finally, the last interrogation window was set to $32 \times 32 \text{ pixel}$ to further increase the spatial resolution of the velocity field. In all passes, an overlap of 50 % of the interrogation window size was used.

It is important to emphasize that spatial resolution cannot be increased unconditionally but must adhere to certain limitations. Typically, a standard PIV analysis is designed to achieve a particle displacement between frames A and B ranging from 5 to 10 *pixels*, a criterion that was also maintained in this study (with an average displacement of 7 *pixels*). A general rule of thumb for selecting the interrogation window sizes is that the final pass should have a window size at least four times larger than the average particle displacement.

Once the analysis is complete, it is necessary to apply the image calibration to define the spatial resolution, convert from pixels/mm to physical units such as m/s, and define the time step between the images of a frame. This information was known from the previous measurement, in which the time interval between frame A and B was set. Additionally, a photo of a ruler was taken to determine the number of pixels corresponding to a known length.

After that, some erroneous vectors might appear due to poorly illuminated regions in the image or strong out-of-plane flow.

To filter out spurious data, the velocity-based approach provided by PIVlab was used, which, by setting velocity limits, removes those vectors whose magnitude falls outside these limits.

Chapter 3

Inlet flow characterisation

As previously stated, a flow characterisation in the inlet of the test section is necessary to understand whether it meets the uniformity requirements needed for the application.

For this reason, this section will aim to provide the most accurate description of the flow possible, considering the main quantities that characterize it, and will seek to answer the question of whether this flow and therefore the wind tunnel, can be used to test the ion thruster.

3.1 Velocity and turbulence uniformity

This section aims to provide a mapping of the velocity profile and turbulence intensity at the exit section to demonstrate that the flow generated by the blower and introduced into the wind tunnel meets fundamental uniformity requirements.

For these measurements, a Pitot tube connected to the Valydine pressure transducer (duly calibrated before acquisition) was used, which, in turn, sent the data through the National Instruments (NI) acquisition board. To carry out these evaluations, the exit cross section was virtually divided into twenty cells (enough to provide an estimate of the uniformity), five on the horizontal side and four on the vertical one. The results are shown in Figure 3.1 and Figure 3.2.

From Figure 3.1, it can be observed that the velocity profile is uniform in both the vertical and horizontal directions of the test section, with a maximum variation of about 0.1 m/s.

From Figure 3.2, relatively low turbulence intensity values can be observed, well below 1%, and it is quite uniform in the exit section.

It is well known from the literature that the Pitot tube is not commonly used for calculating turbulence intensity, a quantity that requires the use of advanced, more precise, and accurate instruments such as hot-wire anemometers.

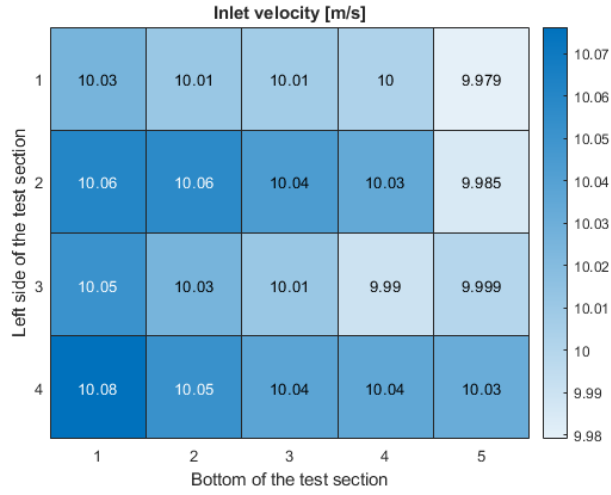


Figure 3.1: Inlet velocity profile

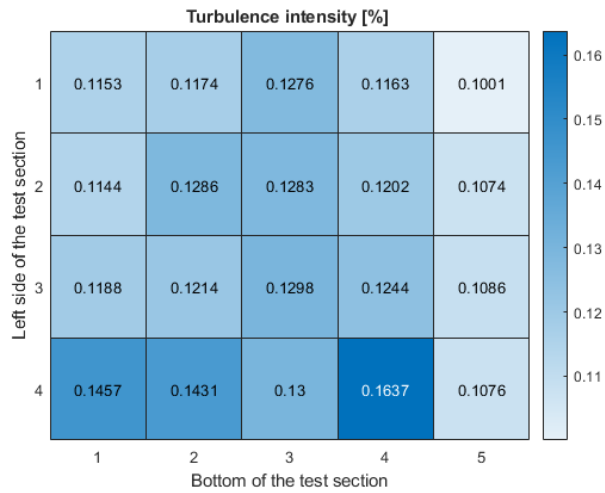


Figure 3.2: Inlet turbulence intensity

However, in this context, the focus is not on the exact calculation of the turbulence level, but rather on obtaining an estimate of the order of magnitude to demonstrate that it remains within certain limits, so as not to significantly affect the flow itself and the experiments that will be conducted on it.

3.2 Temperature uniformity

This part aims to provide a mapping of the temperature distribution in the outlet section through multiple combinations, obtained by varying the power supplied to the electrical resistance and the flow velocity, and then analyse the results and draw some conclusions.

Measurements were carried out as follows: the blower was turned on and set to a certain speed, and simultaneously, the electrical resistance was activated at the desired power level, remaining operational until the steady-state condition was reached. Then, for each reference station, the probe was inserted into the test section, and after waiting for the necessary time, the data acquisition lasted for one minute.

Six cases were analysed, combining three speeds (0, 5 and 10 m/s) with three power levels (0, 60 and 90%); the results are reported below.

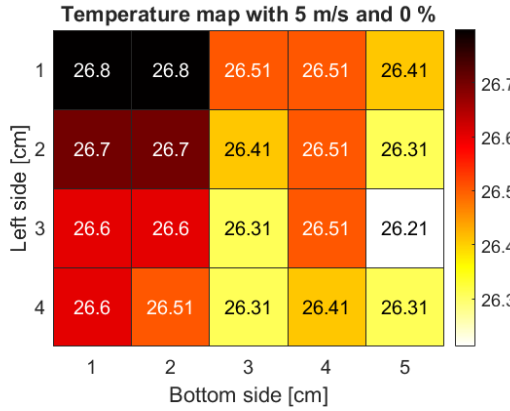


Figure 3.3: 5 m/s, 0% of power

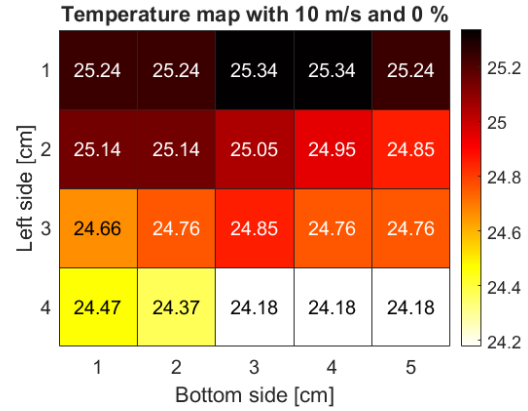


Figure 3.4: 10 m/s, 0% of power

From Figure 3.3 and Figure 3.4, it can be observed that, without the resistance, temperature distribution looks very uniform, with a maximum variation of about one degree. This means that temperature-related flow properties (density, dynamic and kinematic viscosity), at least in this case, can be considered constant in the inlet. However, from Figure 3.4, it is possible to infer the presence of a slight density variation that manifests in three distinct horizontal bands.

The comparative analysis between the temperature maps at the same speed shows how the increase in the resistance power significantly raises the internal temperatures and creates less uniform heat distributions: in Figure 3.5 and Figure 3.6, it can be observed that the map with 60% power presents a more uniform heat distribution, with a less pronounced temperature gradient, unlike the case with 90%, which shows a sharper gradient (Figure 3.7 and Figure 3.8).

Gradient and variance calculation can be an effective method to analyse the

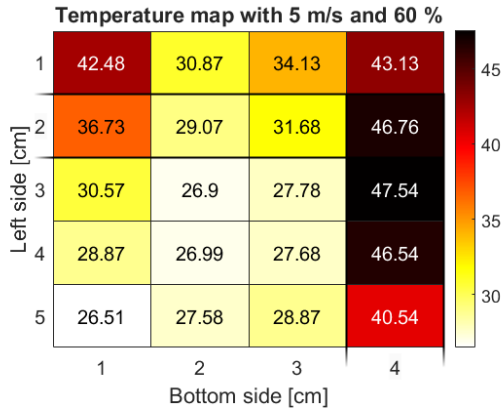


Figure 3.5: 5 m/s, 60% of power

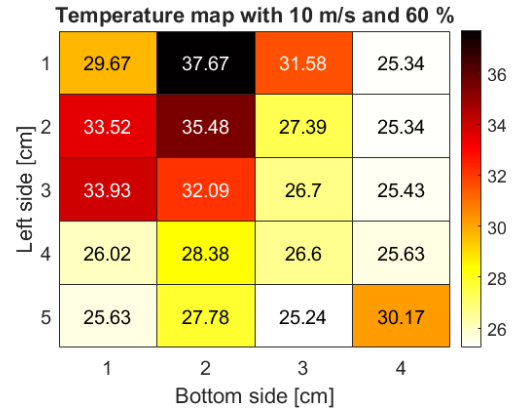


Figure 3.6: 10 m/s, 60% of power

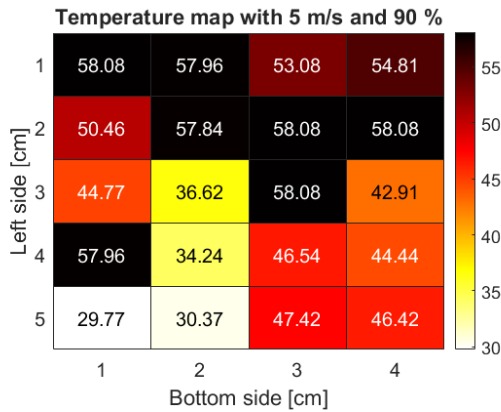


Figure 3.7: 5 m/s, 90% of power

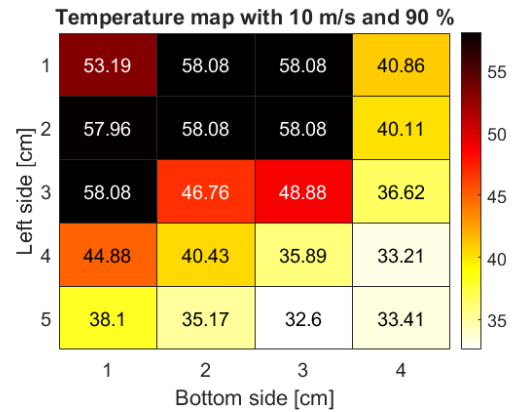


Figure 3.8: 10 m/s, 90% of power

heat distribution and temperature uniformity in the test section.

Variance, indeed, is a measure of how much the values of the temperature gradient module deviate from their mean value. A low variance suggests that the temperature variation is quite uniform, with no regions exhibiting significant changes; on the contrary, a high variance would suggest that there are areas on the map where temperature changes rapidly and others where it changes very slowly.

In this context, at the same speed and for both cases, it can be observed that an increase in resistance power results in a significant increase in variance, as can be seen in Table 3.1.

At the same time, comparing cases with different flow speeds at constant power clearly shows that the airflow speed significantly impacts the temperature distribution in the test section. With a lower speed (5 m/s), heat tends to concentrate more easily, leading to higher temperatures and a less uniform distribution. The

Table 3.1: Mean gradient and variance for every temperature map combination

V \ P	0 %	60 %	90 %
5 m/s	$\nabla_{mean} = 0.1267$ $var = 0.004$	$\nabla_{mean} = 8.24$ $var = 32.72$	$\nabla_{mean} = 9.21$ $var = 49.69$
10 m/s	$\nabla_{mean} = 0.3514$ $var = 0.0215$	$\nabla_{mean} = 3.8$ $var = 5.16$	$\nabla_{mean} = 8.36$ $var = 23.08$

case at 10 m/s, on the other hand, shows a more uniform heat distribution, with a less pronounced thermal gradient compared to the 5 m/s case. This is due to the more intense convective effect occurring at higher speeds, where rapidly moving air removes and transfers heat more efficiently.

3.3 Humidity uniformity

The primary objective of this section is to provide a humidity distribution map in the test section since the process that enabled the correct adjustment of the humidifier to achieve a steam ejection that ensures constant humidity within the area of interest has already been discussed.

Regarding uniformity, two mappings of relative humidity in the test section were developed: one with the humidifier off and a flow speed of 10 m/s, and a second with the same flow but with the humidifier on.

In this case, only 9 measurements were taken on a 3×3 grid. For this reason, the same grid used in the previous cases (velocity, turbulence intensity, and temperature) was not applied. However, to obtain a more homogeneous mapping, interpolation was applied to the missing data. The result is shown in Figure 3.9 and Figure 3.10.

From the Figure 3.9, it can be seen that in the absence of vapor, the humidity distribution within the test section is relatively uniform, with a maximum variation of less than 1%.

In contrast, the Figure 3.10 highlights a significant increase in humidity, showing a strongly non-uniform distribution with pronounced gradients between different areas of the test section.

This demonstrates the need to address humidity formation within the chamber to achieve a greater level of uniformity.

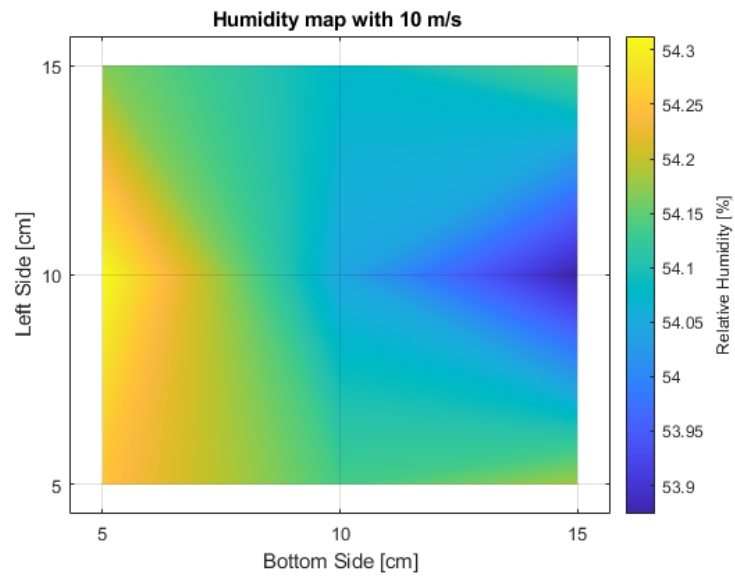


Figure 3.9: Humidity map without humidifier

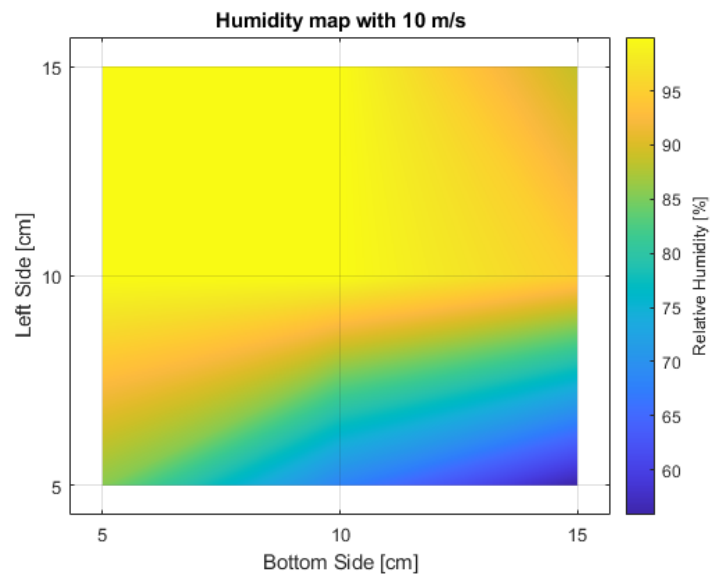


Figure 3.10: Humidity map with humidifier

Chapter 4

Results

4.1 Theoretical background on thrust calculation

Three of the four above-mentioned performance parameters directly depend on the thrust generated by the thruster, thus it becomes necessary to dedicate a section to the methodologies by which this parameter can be measured.

In literature, there are mainly two methods to calculate thrust, one direct and the other indirect: the first, the most straightforward, is called *Force Balance System* and consists, as the name suggests, in connecting together the thruster and a precision balance capable of measuring directly the propulsive force generated

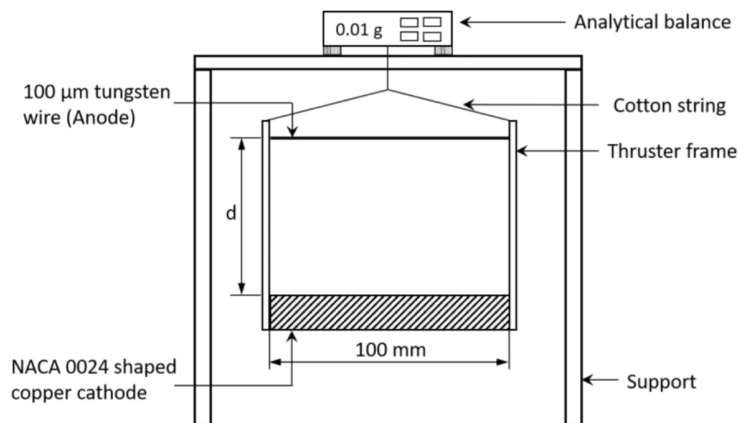


Figure 4.1: Force Balance system experimental setup [44]

It is important to underline that, in this case, the wires connecting the thruster to the entire structure are chosen in such a way as to influence the measurement process as little as possible: they must, therefore, be made of a non-conductive material and have a negligible weight, which is why such wires are often made of

nylon or cotton [8, 10, 45, 5, 14].

The same principle has been used by Kahol et al. [1] who, however, developed a different type of facility consisting of three identical load cells able to provide a good degree of accuracy

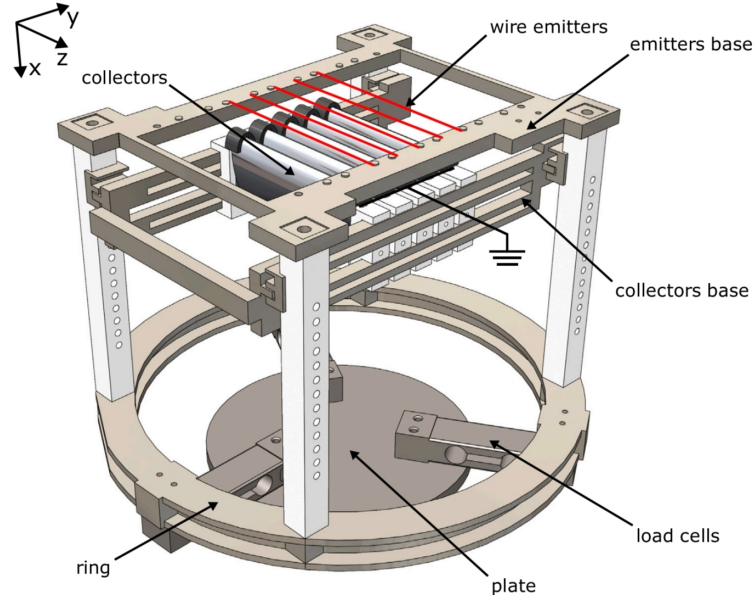


Figure 4.2: Three load cells experimental setup [1]

The second method, on the other hand, is based on analytical models, more or less complex, which attempt to describe the corona effect thrust generation process and which take into account, at the same time, the effect of the aerodynamic drag generated by the collector.

The main models developed in recent years are mentioned below.

In 2020, Vaddi et al. [44] developed and validated, by comparing with experimental data, a 1D model formulation for measuring the thrust: the force induced by an EHD thruster can be computed as the Coulomb force acting on the volume of fluid due to the concentration of ions between the anode and cathode:

$$F_{EHD} = \int \rho_q E d\Omega = \frac{Id}{\mu_b} = \frac{9d\epsilon(V_a - V_0)^2}{8L_c^2}$$

where ρ_e is the charge density, E is the electric field imposed between the two electrodes, I is the current intensity, d is the gap, μ_b is the ion mobility, ϵ is the permittivity of air, V_a is the applied voltage, V_0 is the corona initiation voltage (minimum required voltage to establish corona effect) and L_c is the characteristic length scale of the problem.

The aerodynamic drag, instead, is calculated by the formula:

$$D = \frac{I_d S_{cross} C_D}{\mu_b A} = \Theta F_{EHD}$$

where A is the corona discharge area, S is the cross-section area of the cathode and C_D is the drag coefficient of the airfoil-shaped cathode.

From this, the thrust 1D model can be derived:

$$T = F_{EHD} - D = (1 - \Theta) F_{EHD}$$

Another 1D analytical model was developed by Homaeinezhad [46] who was able to derive the following formula through the Navier-Stokes equations and the ion transport equation:

$$T = \left[4 \rho S_{cross} \left(\xi \epsilon \mu_b S_{cross} \frac{(V_a - V_0)^3}{d^2} \right)^2 \right]^{\frac{1}{3}}$$

where ρ is the gas density, ξ is a constant determined according to the emitter and collector geometry, whereas the other quantities are the same as the previous formulas.

However, in 2021 Belan et al. [18] developed a two-dimensional analytical model capable of calculating the thrust generated by a single thruster unit using a few easily derived parameters; a year later, this formulation was extended to the calculation of the thrust developed by multiple thruster cells [19].

Since the latter models will be used in the following study to calculate the thrust produced by the thruster, a more in-depth analysis is required in which the main assumptions and mathematical steps will be reported.

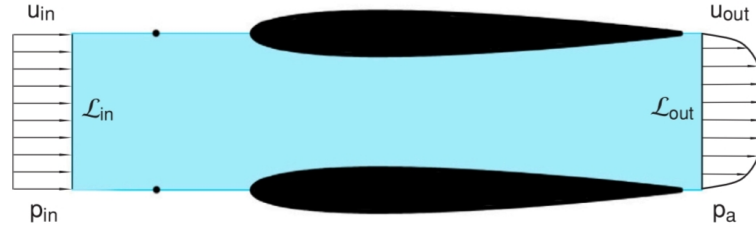


Figure 4.3: Control volume used for thrust calculation [18]

The first model was developed exploiting the momentum conservation integral equation:

$$\begin{aligned} \frac{d}{dt} \iiint_{\Omega} \rho \mathbf{u} \, d\Omega + \iint_{\partial\Omega} \rho \mathbf{u} (\mathbf{u} \cdot \mathbf{n}) \, dS_0 \\ = \mathbf{F}_{visc} - \iint_{\partial\Omega} p \mathbf{n} \, dS_0 + \iiint_{\Omega} \rho \mathbf{g} \, d\Omega + \iiint_{\Omega} \rho_q \mathbf{E} \, d\Omega \end{aligned} \quad (4.1)$$

where ρ is the density of the flow, \mathbf{u} represents the velocity vector, \mathbf{g} is the gravitational acceleration and p is the pressure.

The last term of the equation represents the external force exerted in the control volume by the electric field (E) between the two electrodes on the ions generated by surrounding atmosphere ionisation.

With reference to the Figure 4.3, the following assumptions were used to simplify the problem:

- stationary flow
- gravity term can be neglected
- forces acting on the wire are negligible compared to those acting on the collector
- external viscous forces acting on the free surfaces are neglected because viscosity effects are relevant only near the solid walls of the domain

These hypothesis allow to simplify the Equation 4.1 as follow:

$$\begin{aligned} \iint_{\partial\Omega} \rho \mathbf{u} (\mathbf{u} \cdot \mathbf{n}) dS_0 &= \mathbf{F}_{visc, S_c} - \iint_{S_c} p \mathbf{n} dS_c \\ &+ \iiint_{\Omega} \rho_q \mathbf{E} d\Omega - \iint_{S_b} p \mathbf{n} dS_b \end{aligned} \quad (4.2)$$

where S_0 is the surface of the control volume Ω , S_c is the collector surface, S_b are the free boundaries and \mathbf{n} is the unitary vector normal to each face.

The sum of the aerodynamic forces acting on S_c and the electrostatic forces represents the net force $-R$ experienced by the thruster

$$\iint_{S_0} \rho \mathbf{u} (\mathbf{u} \cdot \mathbf{n}) dS_0 = -\mathbf{R} - \iint_{S_b} p \mathbf{n} dS_b \quad (4.3)$$

Considering line integrals instead of surface ones (2D assumption) and, being concerned with the horizontal component of the equation, the thrust per unit span can be written as a function of the momentum flow and the pressure forces

$$-\frac{R}{b} = \int_{\mathcal{L}} \rho \mathbf{u} \cdot \mathbf{x} (\mathbf{u} \cdot \mathbf{n}) d\mathcal{L} + \int_{\mathcal{L}_b} p \mathbf{n} \cdot \mathbf{x} d\mathcal{L} \quad (4.4)$$

where \mathbf{x} represents the unit vector parallel to the cathode chord and $-\frac{R}{b} = [Drag_{airfoil} + Thrust]$.

If it is assumed that the flow incident on the thruster is aligned to \mathbf{x} direction, the line integral on the control volume contour can be simplified as follow:

$$\int_{\mathcal{L}} \rho \mathbf{u} \cdot \mathbf{x} (\mathbf{u} \cdot \mathbf{n}) d\mathcal{L} = \int_{\mathcal{L}_{out}} \rho u_{out}^2 d\mathcal{L} - \int_{\mathcal{L}_{in}} \rho u_{in}^2 d\mathcal{L}$$

Similarly, it is possible to simplify the second line integral and since $\mathcal{L}_{in} = \mathcal{L}_{out} = s$ (spacing, distance between two collectors) the final equation is derived:

$$-\frac{R}{b} = \int_{\mathcal{L}_{out}} \rho u_{out}^2 d\mathcal{L} - \int_{\mathcal{L}_{in}} \rho u_{in}^2 d\mathcal{L} + (p_a - p_{in}) |\mathcal{L}_{out}| \quad (4.5)$$

where p_a is the ambient pressure and p_{in} represents the pressure at the control volume inlet.

The advantage of this equation is that, assuming constant air density, the only unknown quantities are the pressure at the inlet of the control volume and the velocity profile of the flow both in the outlet and in the inlet; these quantities are, however, easy to obtain: assuming a uniform flow, the pressure can be obtained by means of a Pitot tube, thanks to which it is also possible to derive the velocity profile at both the front and rear of the power unit.

Another possible velocity profile measurement technique is PIV which is more complex to implement than the Pitot tube but offers numerous advantages: first of all, this technique provides a more comprehensive 2D view of the velocity profile, moreover, contrary to the Pitot tube, it is a non-intrusive technique and does not interfere in any way with the evolution of the flow around the thruster.

The two-dimensional model just described was subsequently revisited in favour of a 3D reformulation of the momentum conservation on a volume enclosing the thruster, shown in Figure 4.4

In this case, the contribution of all thruster units was also taken into account, as well as that produced by the outer regions, whose contribution becomes negligible as the number of thruster units (n_c) grows:

$$R = n_c \left[\iint_{\mathcal{S}_{out}} \rho u_{out}^2 dy dz - \iint_{\mathcal{S}_{in}} \rho u_{in}^2 dy dz + (p_a - p_{in}) |\mathcal{S}_{out}| \right] + R_{outer} \quad (4.6)$$

Although such an improved model provides more accurate results, it requires knowledge of $u(y, z)$, i.e. a two-dimensional velocity profile both at the inlet and the outlet of the control volume; this is only possible by using the PIV technique.

4.2 Analysis of the current case without plasma creation

Despite the greater difficulty of implementation, PIV was chosen as the method for measuring the velocity profile at the inlet and outlet in the current setup; this

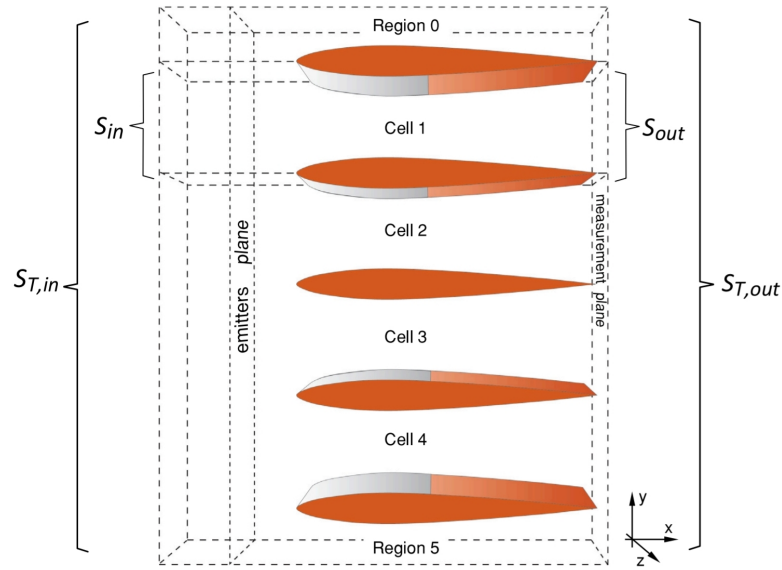


Figure 4.4: Control volume used for thrust calculation [19]

decision was also made with a future perspective in mind since the use of a Pitot tube would have led to some problems: in addition to being an intrusive method, this probe is made of metal, and since the goal is to generate propulsion through a strong electric field, it needs to be grounded, which is not easy to implement.

However, to be able to use this technique in the future for calculating the thrust produced by the ion thruster, it is necessary to demonstrate its feasibility in the current test section. In this regard, it is also essential to show that the Equation 4.5 produces correct results by taking the velocity field values obtained from the PIV as input.

For this reason, and since the ion thruster prototype was not yet ready to be used, the tests on the possibility of implementing this technique and validating the formula were carried out on a 3D-printed NACA0012 airfoil. The airfoil has a chord of 6 cm and a span of approximately 19.5 cm, which is 97.5% of the width of the test section, in order to avoid the formation of three-dimensional effects due to the finite length of the airfoil.

It is important to note that, in the absence of an electric field and therefore plasma generation, the contribution of thrust to the resulting force R is zero, and the latter consists solely of the drag generated by the airfoil itself, thus equal to Equation 4.5 but with $R = D$.

The ultimate goal, therefore, was to calculate, using the aforementioned technique and formula, the drag of the airfoil in a low Reynolds number environment (on the order of $Re \sim 10^4$) and subsequently derive the drag coefficient C_D for the



Figure 4.5: Airfoil tested inside the test section

conditions under consideration. To validate the results and the methodology used, the drag coefficient was then compared with results already available in the literature for the same airfoil subjected to the same Reynolds number as the test performed.

What has been described is not only a way to demonstrate the feasibility of the technique, but is also fundamental for the future calculation of the actual thrust generated by the ion thruster. As already stated, from the formula Equation 4.5, it is clear that the resulting force R , which can be calculated by using the PIV results as input, is the sum of two contributions: the thrust generated by the ionization of the atmosphere and the subsequent acceleration of ions, and the drag produced by the thruster itself. It is, therefore, crucial to be able to isolate the latter in the absence of plasma, so that it can be subtracted from the resulting force in order to determine the actual thrust generated by the thruster.

At this point, it is necessary to analyze in more detail two of the three contributions from the Equation 4.5: the one related to the incoming flow into the control volume and the contribution concerning the pressure difference between inlet and outlet.

As reported in section 3.1 and concerning the velocity and turbulence intensity

mapping, it is possible to assume a constant inlet velocity profile along the vertical direction. This allows for further simplification of the problem, because by applying the continuity equation to the reference domain, a constant inlet velocity value can be derived solely from the knowledge of the velocity profile downstream of the airfoil.

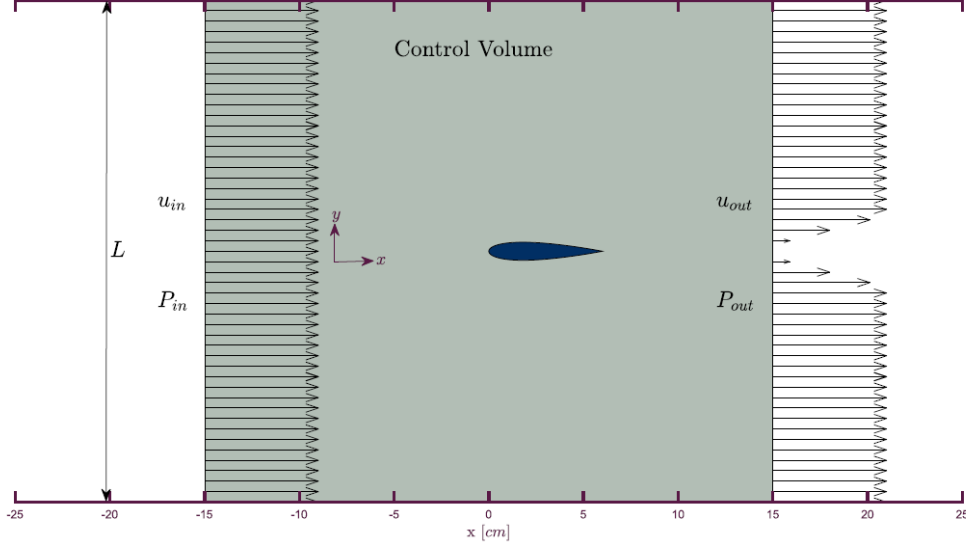


Figure 4.6: Arbitrary control volume for x-momentum calculation

For a steady flow the continuity equation states:

$$\iint_S \rho \mathbf{u} \cdot \mathbf{n} dS = 0$$

With reference to Figure 4.6, remaining within the 2D assumption and recalling that the integral is zero on the airfoil surface due to the no-slip condition, it is possible to expand the integral and write:

$$\int_{\mathcal{L}_{out}} \rho \mathbf{u} \cdot \mathbf{n} d\mathcal{L} + \int_{\mathcal{L}_{up}} \rho \mathbf{u} \cdot \mathbf{n} d\mathcal{L} + \int_{\mathcal{L}_{in}} \rho \mathbf{u} \cdot \mathbf{n} d\mathcal{L} + \int_{\mathcal{L}_{down}} \rho \mathbf{u} \cdot \mathbf{n} d\mathcal{L} = 0$$

Finally, assuming that the vertical velocity component is zero along both the upper and lower sides, it is possible to retrieve the inlet velocity profile:

$$u_{in} = \frac{1}{L_{in}} \int_{\mathcal{L}_{out}} u_{out} d\mathcal{L} \quad (4.7)$$

This proves to be a useful simplification of the problem, as it reduces the number of variables to measure, allowing the PIV technique to be applied only in the downstream part of the airfoil.

However, it is important to remember that the flow measurements around the airfoil are carried out inside a test section that surrounds the airfoil itself: that is why it is essential to account for wall interference and to use a blockage-correction method.

The research [47] recommends using the classical method, which will be briefly illustrated below.

It states that the blockage interference around the airfoil arises from two contributions: the model itself and its wake. The first one is described by:

$$\epsilon_s = 0.524 \left[1 + 1.2\beta \left(\frac{t}{c} \right) \right] \frac{S_{cross}}{\beta^3 h^2} \quad (4.8)$$

where A denotes the cross-sectional area of the airfoil, h is the height of the test section, t/c is the thickness-to-chord ratio of the airfoil and $\beta = \sqrt{1 - M^2}$ is the Prandtl-Glauert factor to account for the compressibility (M stands for Mach number).

The second contribution, instead, is described by:

$$\epsilon_w = 0.25 \left(\frac{c}{h} \right) \frac{1 + 0.4M^2}{\beta^2} C_D \quad (4.9)$$

where C_D denotes the drag coefficient of the airfoil calculated with the no-blockage case.

Therefore, speed must be corrected according to:

$$U_c = U_u(1 - \epsilon_t) \quad (4.10)$$

where $\epsilon_t = \epsilon_s + \epsilon_w$.

Another key aspect in obtaining accurate results concerns the term related to the pressure difference in the Equation 4.5. A precise and accurate measurement of the pressure difference between the inlet and outlet is crucial because it represents the largest contribution in the aforementioned formula, as the two components resulting from the upstream and downstream velocities are comparable to each other, and their difference tends to be almost zero.

This term, in turn, is the sum of two contributions: one related to the pressure losses caused by the presence of the airfoil, and the other due to the pressure losses caused by the test section in which the measurements were carried out.

$$\Delta p = p_{out} - p_{in} = \Delta p_{airfoil} + \Delta p_{ts} \quad (4.11)$$

For a fully developed flow, the pressure losses inside a square duct can be easily obtained using the Darcy-Weisbach equation [48]:

$$\Delta p_{ts} = f \left(\frac{L}{D_h} \right) \frac{\rho U^2}{2} \quad (4.12)$$

where $D_h = (4 \cdot Area)/(Perimeter)$ is the hydraulic diameter, f is the friction factor obtained from the Moody diagram and L is the length of the duct involved, namely the distance between the inlet and the outlet.

The critical aspect, however, concerns the evaluation of the first contribution, namely the one due to the losses caused by the airfoil. By using the continuity equation to estimate the inlet velocity profile based on the measured outlet profile, there is no defined inlet station where pressure can be measured; this, combined with the absence of wall-mounted pressure tabs upstream of the airfoil, made the pressure measurement at the inlet very difficult.

On the other hand, the pressure measurement downstream of the airfoil was performed using the pressure tab located 15 cm (2.5 times the chord length) from the trailing edge of the airfoil and, consequently, the $2D$ velocity profile at the outlet, obtained through PIV, was selected at the same point.

To overcome this problem, as a first approximation, the conservation of total pressure along a streamline around the airfoil was assumed:

$$p_{out} - p_{in} = q_{in} - q_{out} \quad (4.13)$$

In this formula, the dynamic pressure at the inlet is easily obtained since the flow is incompressible, meaning the density is known, and the velocity has been calculated using the Equation 4.7. The dynamic pressure at the outlet, on the other hand, is measurable: the presence of a pressure tab in the settling chamber allows the total pressure to be determined, thus by measuring the pressure difference between this pressure tab and the one positioned downstream of the airfoil, the value of q_{out} can be obtained.

Finally, it is important to emphasize that the absence of a pressure measurement station at the inlet also affects the calculation of losses along the duct, as the relevant formula requires knowledge of the length of the test section over which these losses are to be calculated. In this case, an imaginary reference station was assumed, located 6 cm upstream of the leading edge. This theoretical distance was chosen because, at that point, the airflow would not be influenced by the airfoil itself, allowing the assumption of a uniform velocity profile along the vertical side to remain valid.

4.3 Experimental Results

This section's primary goal is to present the results obtained by applying the PIV optical technique to the previously described setup, followed by an analysis of these results and drawing conclusions.

Before proceeding, however, it is necessary to make a premise regarding the manner in which the results were obtained and the associated timing. As already

mentioned, the correct execution of the technique was not immediate; numerous issues arose during the process and were gradually resolved, thus improving the setup. Although known and studied before the PIV application, the factors addressed in subsection 2.5.4, and the respective conclusions, are the result of numerous unsuccessful tests, which at times produced outcomes completely inconsistent with the physical phenomenon. Other times, the results were more consistent but still incorrect when compared to existing research, while some tests produced images with poor resolution, making them unusable for analysis.

The best setup for studying the phenomenon, adhering to the conditions discussed in the previous section, was achieved only after multiple attempts, and this took a significant amount of time.

One of the first tests performed, in fact, showed extremely low spatial resolution, and the displacement vectors contain numerous outliers despite using the POD filter as pre-processing and the velocity-based method as post-processing. As can be seen from Figure 4.7 there are black areas with no vectors, and the images have an average Validation Detection Probability (VDP) of 64%.

The VDP is defined as the probability that the highest correlation peak obtained from the cross-correlation between two successive frames corresponds to the actual average displacement of the set of particle images. It is an index of how many displacement vectors were validated during post-processing compared to how many were deemed unreliable. A high VDP is essential to ensure the accuracy of the displacement vectors [49].

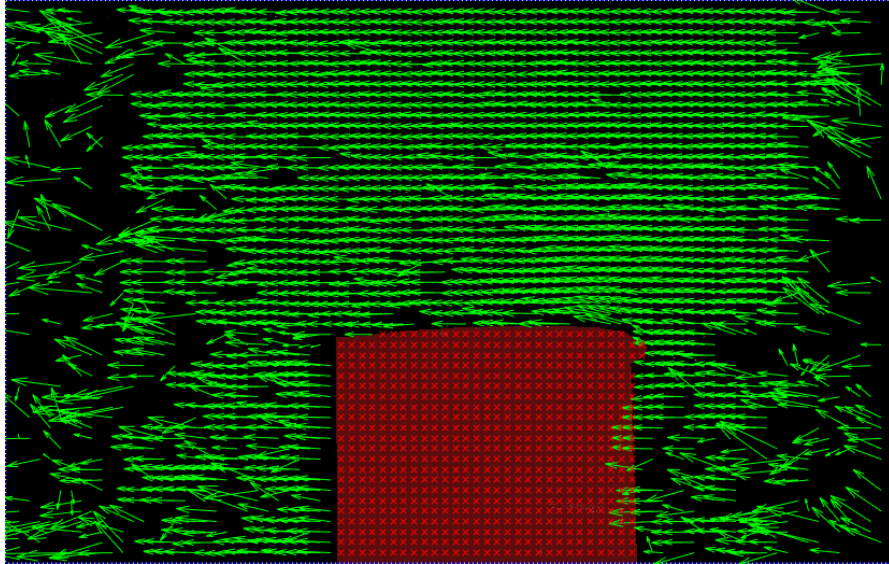


Figure 4.7: Displacement vectors field with a $VDP = 63.9\%$

Once the average was taken over all the acquired images (315 in total), the

velocity field was computed.

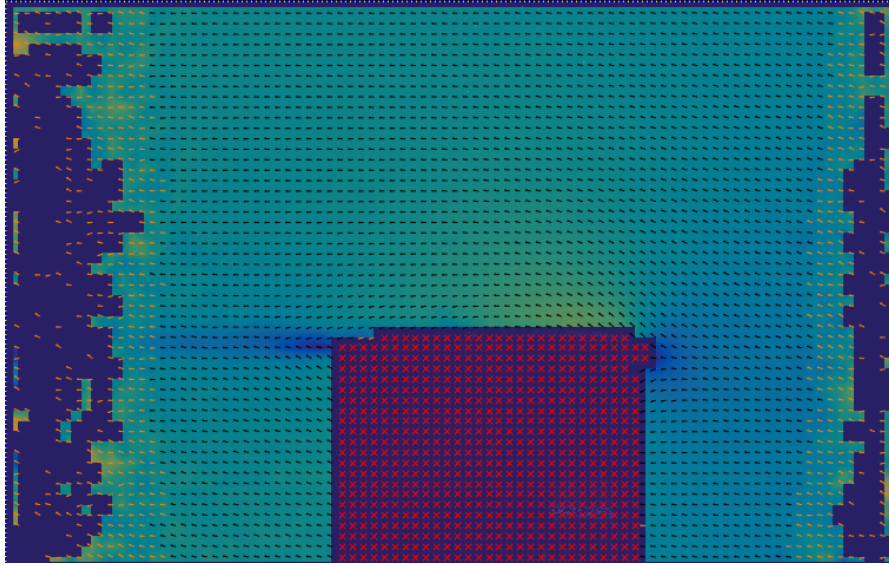


Figure 4.8: Velocity magnitude field

The Figure 4.8 shows numerous dark blue patches where velocity-defining vectors are absent, indicating that the software, due to low resolution, was unable to calculate the velocity field, even after interpolating the data obtained from the analysis (orange vectors in the image). Furthermore, from this figure and the previous one, it can be observed that there is a large red area in the central part. This is nothing more than a mask applied during the pre-processing phase to exclude the computation of the cross-correlation in the mentioned area, which is characterized by the presence of the airfoil profile as well as poor illumination in the lower part due to the profile itself. The use of this mask will also be visible in the subsequent images for the cases that will be presented.

For the sake of curiosity, an airflow velocity profile was extrapolated downstream of the airfoil. The Figure 4.9 not only presents a discontinuity, which is not physically possible, but it also lacks the characteristic wake that typically appears in the rear of an airfoil in a viscous flow. Therefore, this velocity field is not an accurate representation of what is actually happening inside the test section.

It is commonly known that the study of the drag produced by a body immersed in an airflow strongly depends on the Reynolds number associated with the flow. Consequently, to validate the results obtained during this experiment, it is necessary to compare them with previous research characterized by the same airfoil profile and Reynolds number (or at least the same order of magnitude).

In this context, given the properties of the airflow and the geometry of the profile (NACA 0012, chord $c = 6 \text{ cm}$), the reference dimensionless parameter could only

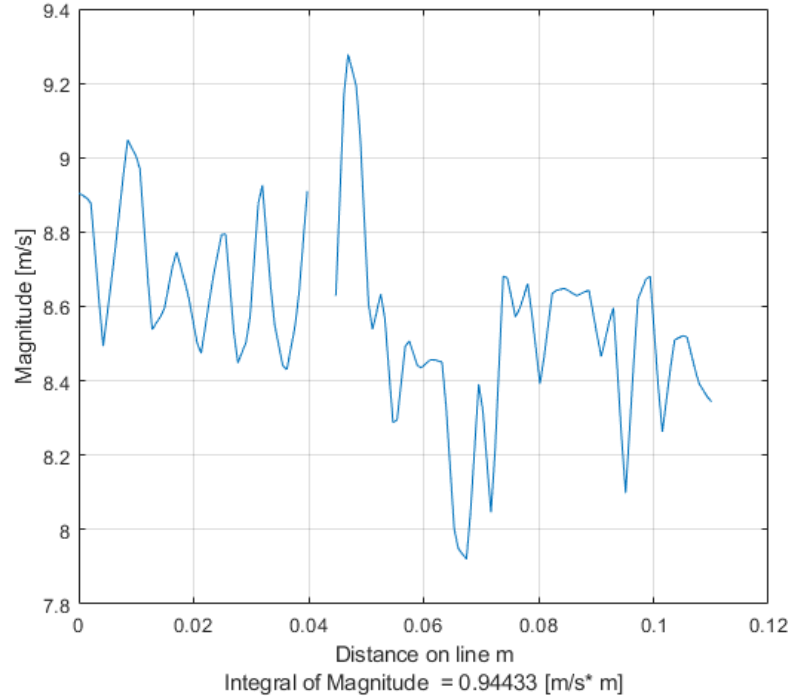


Figure 4.9: Velocity profile downstream

be varied by changing the wind tunnel's operating velocity. As already mentioned, the maximum velocity of the facility is 15 m/s , which corresponds to a Reynolds number approximately equal to:

$$Re = \frac{\rho U c}{\mu} = \frac{1.225 \cdot 15 \cdot 6 \cdot 10^{-2}}{1.72 \cdot 10^{-5}} \approx 6.4 \cdot 10^4 \quad (4.14)$$

where ρ is the air density, U is the velocity, μ is the air dynamic viscosity, and where all the standard values are considered.

Unfortunately, in the literature, only few studies on the drag produced by the NACA 0012 profile at low Reynolds numbers (on the order of 10^4) were identified. Therefore, only three cases will be analysed and compared with the findings of this study.

Case 1: $U_{mean} = 2.8 \text{ m/s} \rightarrow Re \approx 1.0 \cdot 10^4$

The first case to be examined involves a wind tunnel operating velocity of $U = 2.8 \text{ m/s}$. Unlike what is shown in Figure 4.8, where the entire field of view around the airfoil was analysed, this acquisition focuses only on the downstream

region of the profile because, as mentioned in section 4.2, the calculation of the drag coefficient requires only a velocity profile, characterized by the wake, in the rear part of the profile.

Figure 4.10 shows the displacement vector field associated with this test after applying the POD filter as pre-processing and the velocity-based method as post-processing. The image demonstrates a high spatial resolution, characterized by an average VDP of 95 %, which attests to the quality of the execution of the PIV optical technique.

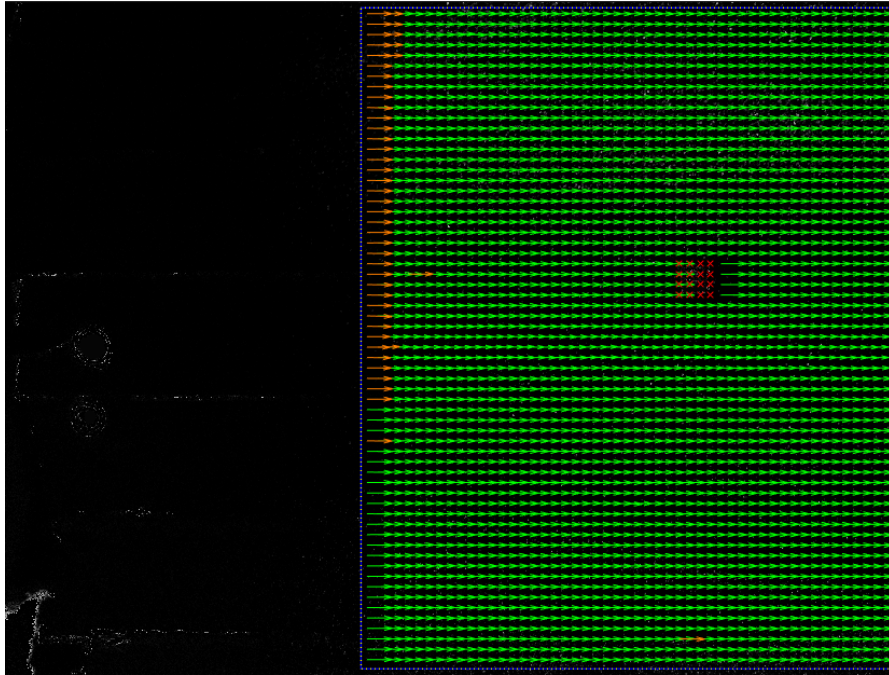


Figure 4.10: Case 1: Displacement vectors field with a $VDP = 95\%$

It is important to point out that the image processing was carried out only on the portion effectively illuminated by the laser (right side). The opposite side, instead, corresponds to the airfoil profile, which in this case was not lighted up and is therefore not visible.

Once the temporal average was computed over all the acquired images (600 in total), the velocity field was obtained. Figure 4.11 clearly shows the presence of a well-defined wake in the downstream region of the airfoil and a fairly uniform velocity field in the areas not influenced by the profile itself.

From this, it is possible to extract a velocity profile along the y -axis at a fixed x -coordinate located one chord length downstream from the trailing edge of the NACA 0012 (Figure 4.12).

From this last image, the presence of a wake caused by the airfoil in the central

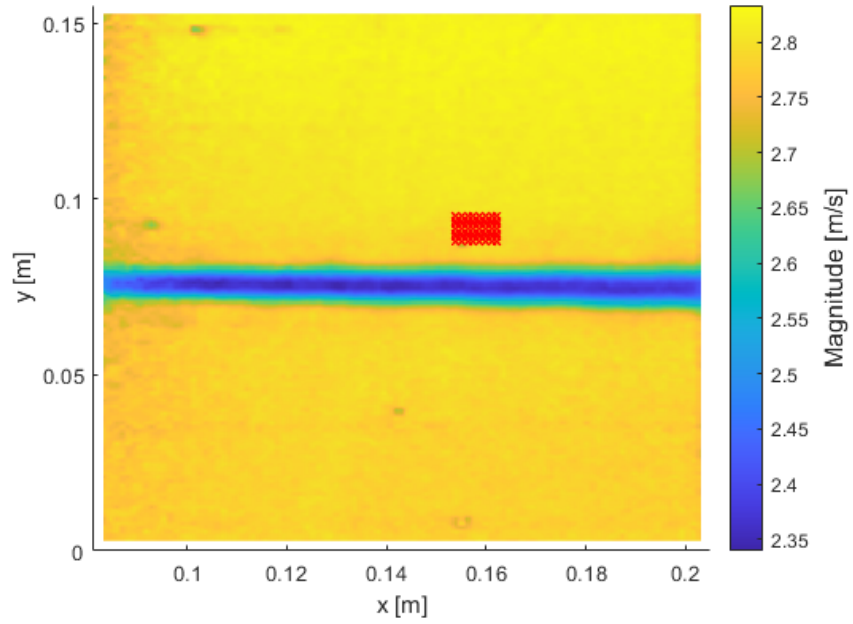


Figure 4.11: Case 1: Magnitude velocity field

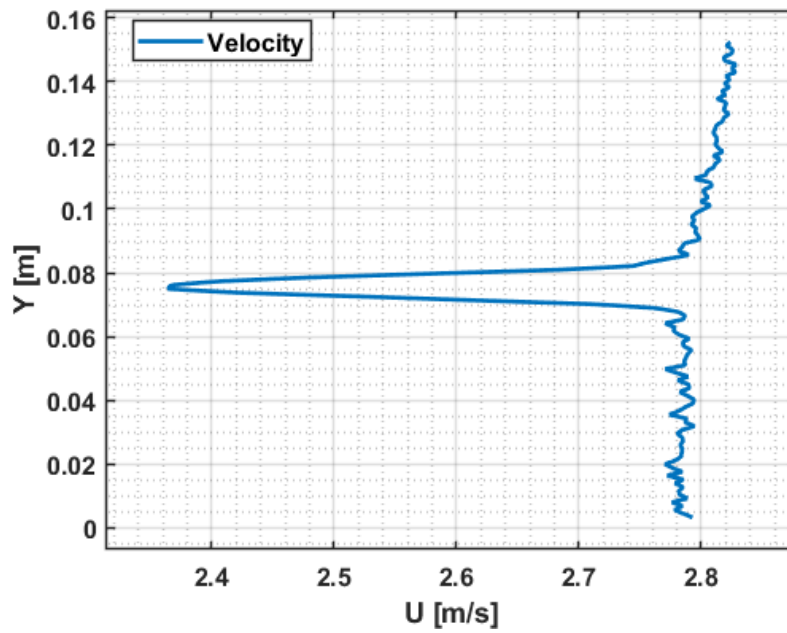


Figure 4.12: Case 1: Downstream velocity profile

part of the field of view is evident. Additionally, two aspects must be highlighted: first, the fluctuations present in the regions outside the wake, which are not influenced by the body, can be attributed to the turbulence intensity. Although low, this still has some influence on the velocity field.

Second, the choice of field of view is noteworthy: it can be observed that the velocity field in the region outside the wake does not show a sudden decrease at the two edges, indicating that the boundary layer formed by the walls of the test section has not been reached.

Moving forward, one of the main concerns when using PIV is the potential occurrence of *Peak Locking*: a systematic issue that arises during the processing of velocity data obtained from images. It consists of a bias in the correlation results, where the particle displacements obtained from the cross-correlation tend to be erroneously favoured toward discrete values (typically integers). This issue is often associated with the use of particles with a diameter that is too small (around 1 pixel), causing the cross-correlation to fail in correctly identifying the peak associated with the true displacement [50]

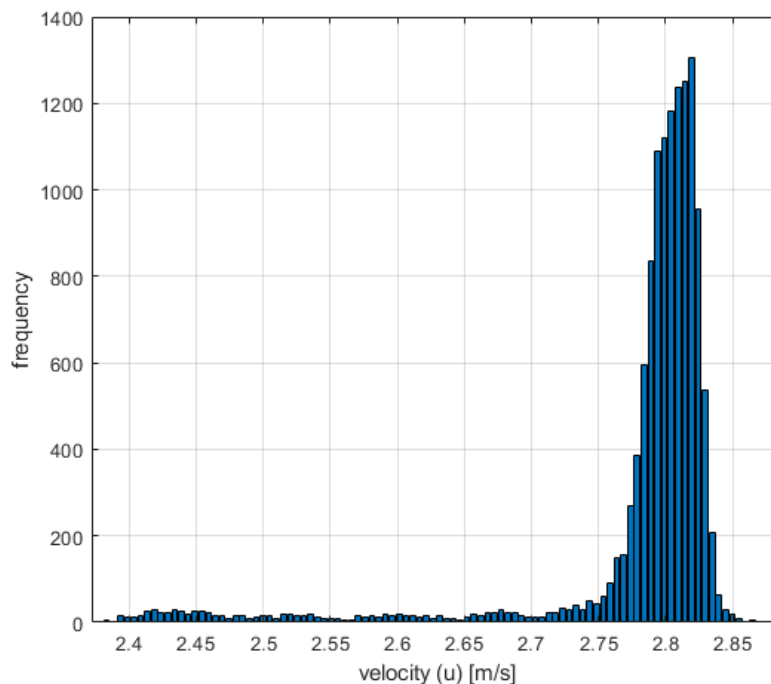


Figure 4.13: Case 1: Histogram of velocities

It is possible to verify that this issue has been avoided by plotting the histogram of all displacements or velocity values. If the histogram predominantly shows

peaks around integer values, it indicates that peak locking has occurred. However, Figure 4.13 demonstrates that, at least in this context, such a phenomenon has been avoided because the graph exhibits a sort of Gaussian distribution, around the average value of $U = 2.8 \text{ m/s}$, which is the speed at which the wind tunnel was set.

At this point, to provide a more comprehensive description of the measurements obtained through the PIV technique, it is possible to illustrate other key characteristics that define the flow under investigation, such as the turbulence intensity, the vorticity, and the divergence of the velocity field.

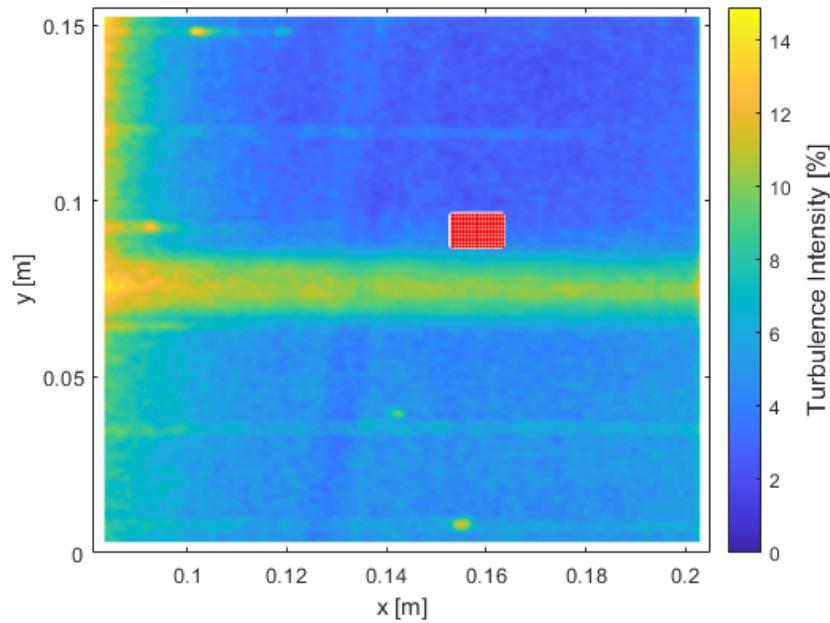


Figure 4.14: Case 1: Turbulence intensity

Figure 4.14 illustrates the characterization of turbulence intensity within the reference domain. First and foremost, the image reveals that, as expected, turbulence intensity is significantly higher within the wake region, reaching a maximum of 14%. At the same time, it is also evident that the presence of the airfoil affects the turbulence intensity across the entire downstream area, not just within the wake region.

However, the high value observed in the upper left part of the field of view is mainly due to poor illumination or a low number of particles in that region, which consequently increased the standard deviation.

The Figure 4.10 indeed shows that, in that specific portion of the field of view, the cross-correlation was unable to compute valid vector displacements, and the

PIVLab software interpolated the missing data (orange vectors in the figure). This inevitably resulted in an incorrect calculation of the turbulence intensity.

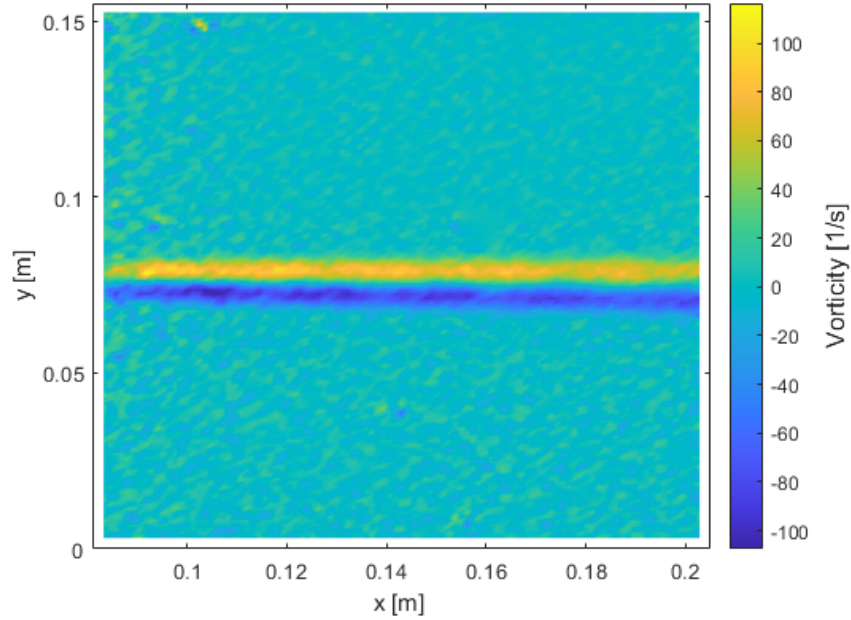


Figure 4.15: Case 1: Vorticity field

Similarly, it is possible to show the mean vorticity that characterizes the flow under investigation. Figure 4.15 demonstrates that vorticity is virtually zero throughout the domain, except for the region associated with the wake. Here, it is clear that most of the vorticity is concentrated along the edges of the wake, where the shear layers are located, namely regions where the velocity changes rapidly until it adjusts to the free stream. In the center, however, the vorticity is practically zero, which is due to the fact that the velocity in this area experiences minimal transverse variation.

Finally, Figure 4.16 shows the divergence of the velocity field associated with the domain under investigation. As expected, this is virtually zero throughout the domain since an incompressible flow has been studied. According to the continuity equation, it is known that if the density is constant, the divergence of the velocity must be zero.

Using the velocity profile from Figure 4.12 and following the steps outlined in section 4.2, it is possible to evaluate the aerodynamic drag and the associated coefficient both for the corrected case and not. The result is presented in Table 4.1

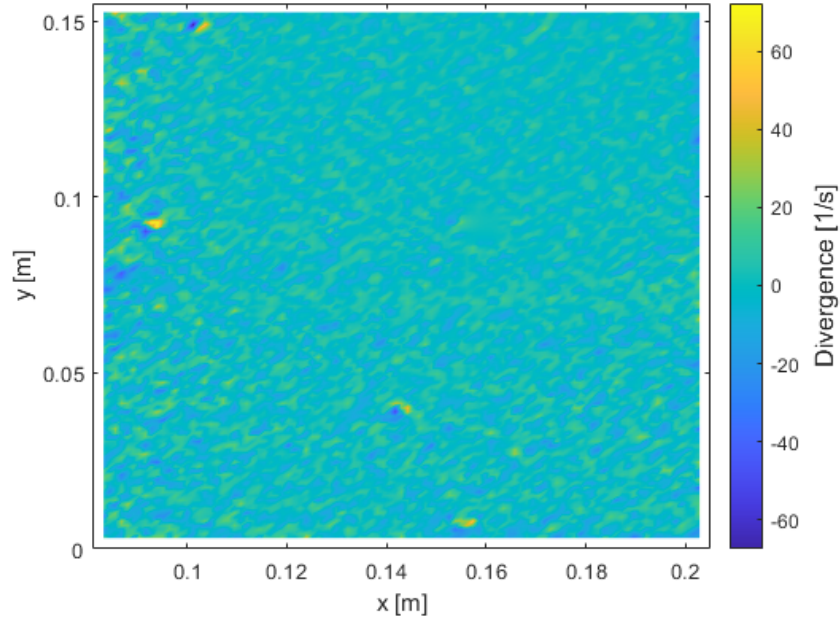


Figure 4.16: Case 1: Divergence field

Case 2: $U_{mean} = 5.8 \text{ m/s} \rightarrow Re \approx 2.5 \cdot 10^4$

The second case to be examined involves a wind tunnel operating velocity of $U = 5.8 \text{ m/s}$, and, as in the previously mentioned analysis, the focus is only on the downstream region of the airfoil profile, as it is the only one required for the calculation of the produced drag.

Figure 4.17 shows the displacement vector field associated with this test after applying the POD filter as pre-processing and the velocity-based method as post-processing. Also, in this case, a high spatial resolution was achieved, characterized by an average VDP of 96 %, a percentage that demonstrates how the cross-correlation developed by the PIVLab software was able to provide reliable results.

Once again, after computing the temporal average over all the acquired images, the velocity field was obtained. Figure 4.18 clearly shows the presence of a well-defined wake in the downstream region of the airfoil and a fairly uniform velocity field in the areas not influenced by the profile itself.

As previously done, from this velocity field, it was possible to extract the velocity profile along the y-axis at a distance of one chord length from the trailing edge of the airfoil. From Figure 4.19, the presence of a wake in the velocity profile is distinctly observable, whereas the velocity remains almost constant in the area unaffected by the NACA 0012 profile, despite the presence of fluctuations that can be attributed solely to turbulence intensity.

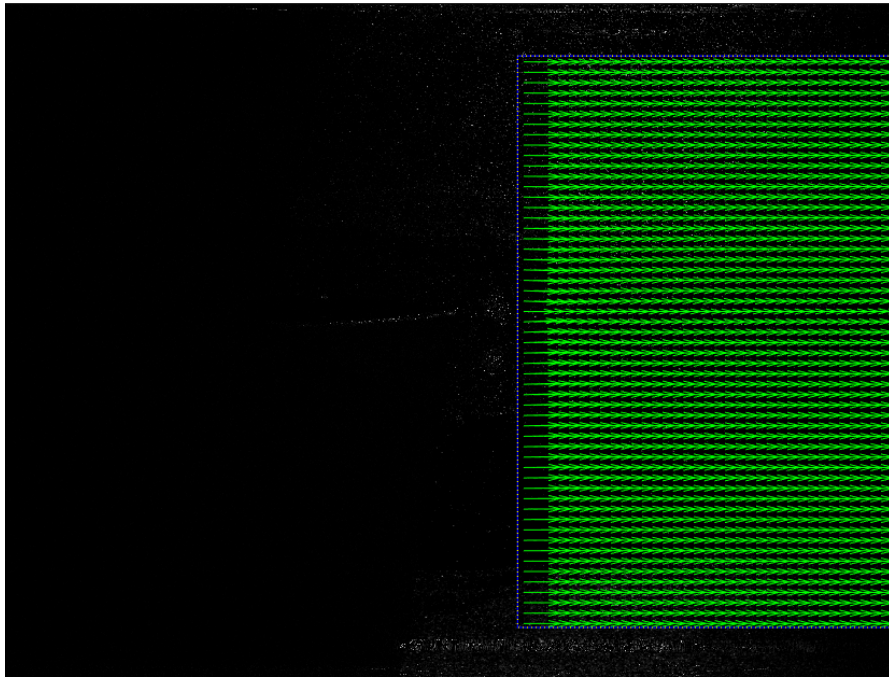


Figure 4.17: Case 2: Displacement vectors field with a $VDP = 96\%$

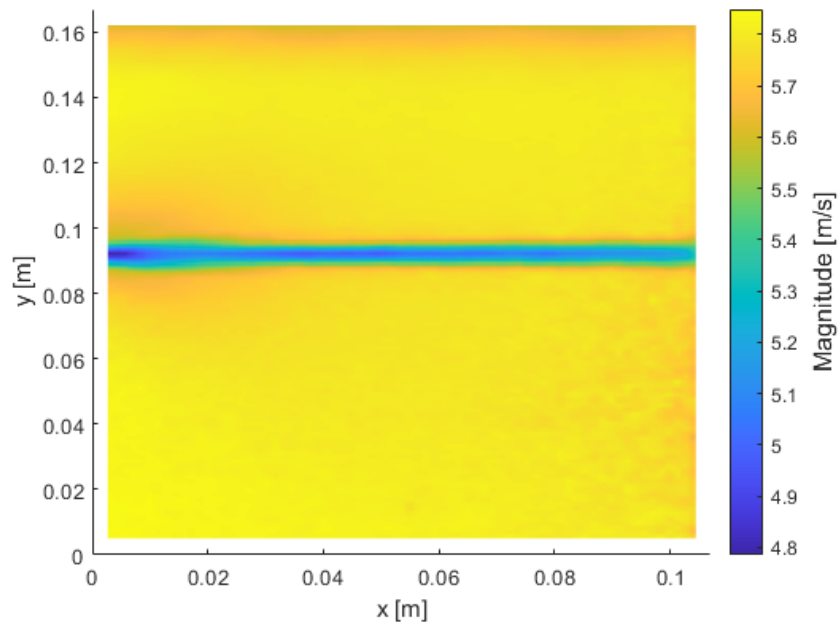


Figure 4.18: Case 2: Magnitude velocity field

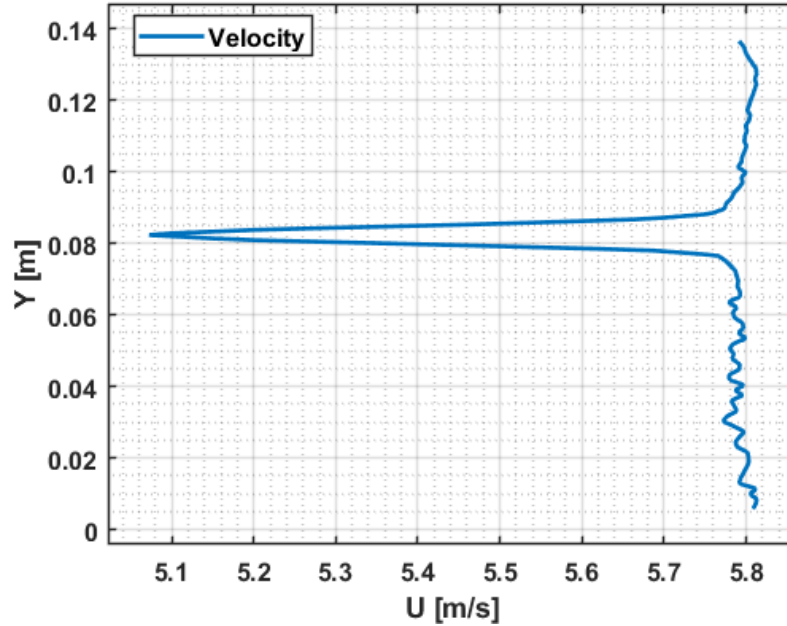


Figure 4.19: Case 2: Downstream velocity profile

Also, for this PIV analysis, it is possible to verify that the Peak Locking phenomenon has been avoided by plotting the histogram of velocity values in relation to the number of occurrences within the field of view. As shown in Figure 4.20, a frequency peak can be observed for the free-stream velocity within the test section, equal to $U = 5.8 \text{ m/s}$, along with the absence of peaks around integer values. This confirms that the phenomenon has not been detected.

For the sake of completeness and to provide a more comprehensive description of the flow analysed by the PIV technique, as in the previous case, the trend of the quantities of main interest will be shown.

Figure 4.21 illustrates the characterization of turbulence intensity within the reference domain.

As in the previous case, and as expected, the turbulence intensity reaches its maximum value, approximately 12 %, in the wake region. At the same time, an overall increase in turbulence intensity can be observed throughout the domain of interest.

However, in the lower right side of the field of view, some values appear inconsistent with the rest of the free-stream region. This is most likely due, once again, to poor illumination or a low number of particles during the PIV analysis, which resulted in velocity vectors characterized by a high standard deviation.

Similarly, it is possible to visualize the mean vorticity that characterizes the

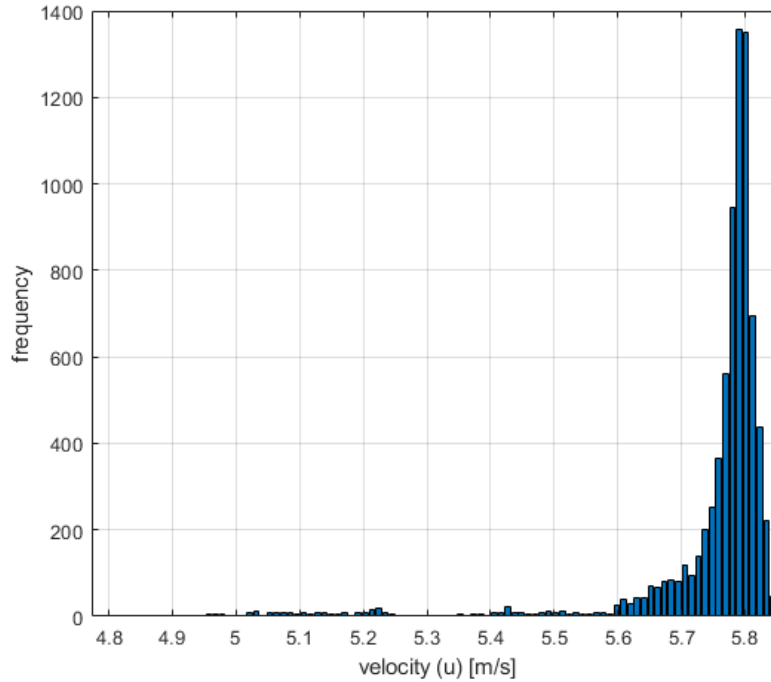


Figure 4.20: Case 2: Histogram of velocities

investigated flow. Figure 4.22 demonstrates that vorticity is virtually zero throughout the domain, except for the region associated with the wake. Specifically, as already observed in the previous case, vorticity is concentrated at the edges of the wake, in the regions of the flow where the velocity gradient is higher.

Finally, Figure 4.23 shows the divergence of the velocity field associated with the domain of interest.

This case is particularly interesting because it highlights one of the potential drawbacks of the optical PIV technique. From the image, it is clearly observable that the flow divergence is not zero within the domain, which is in stark contrast to the theoretical assumption for an incompressible flow.

The PIV technique computes velocity fields through image processing, cross-correlations, and interpolations to obtain spatial derivatives. Consequently, image analysis software often does not account for the physical constraints imposed by the problem, introducing artifacts in the divergence field. To address this issue, the literature presents techniques that utilize penalized and constrained Radial Basis Functions to compute an analytic representation of velocity and pressure fields from noisy and sparse data, regardless of whether they were obtained using cross-correlation or particle tracking algorithms. Essentially, the use of these

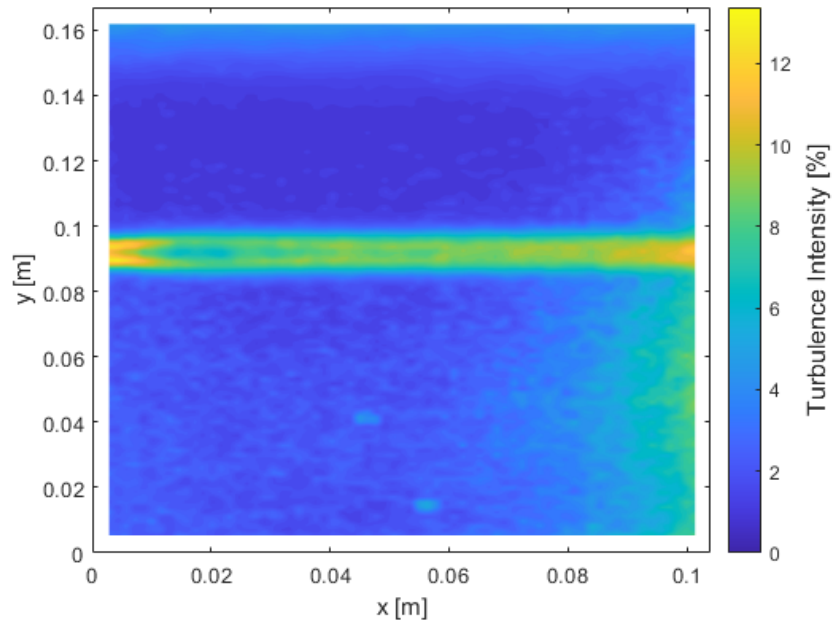


Figure 4.21: Case 2: Turbulence intensity

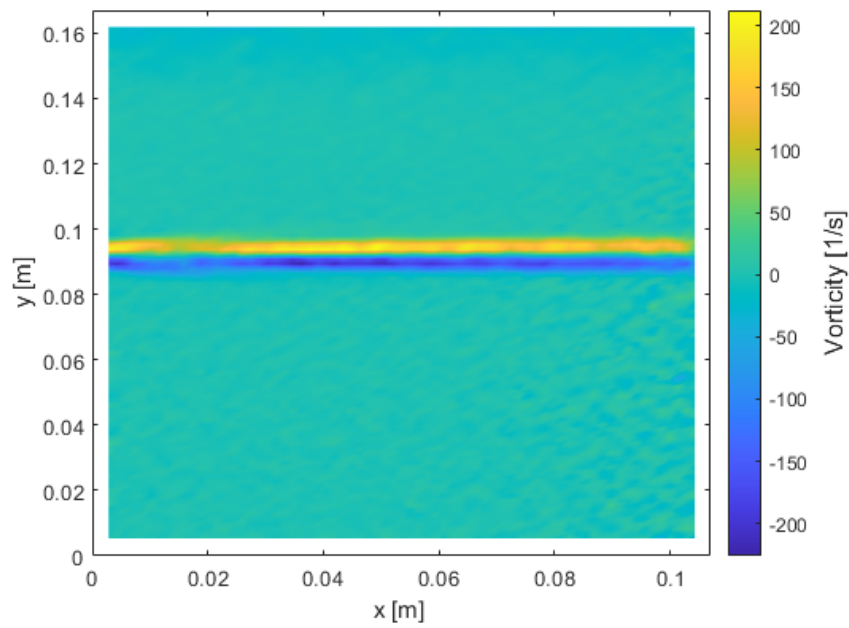


Figure 4.22: Case 2: Vorticity field

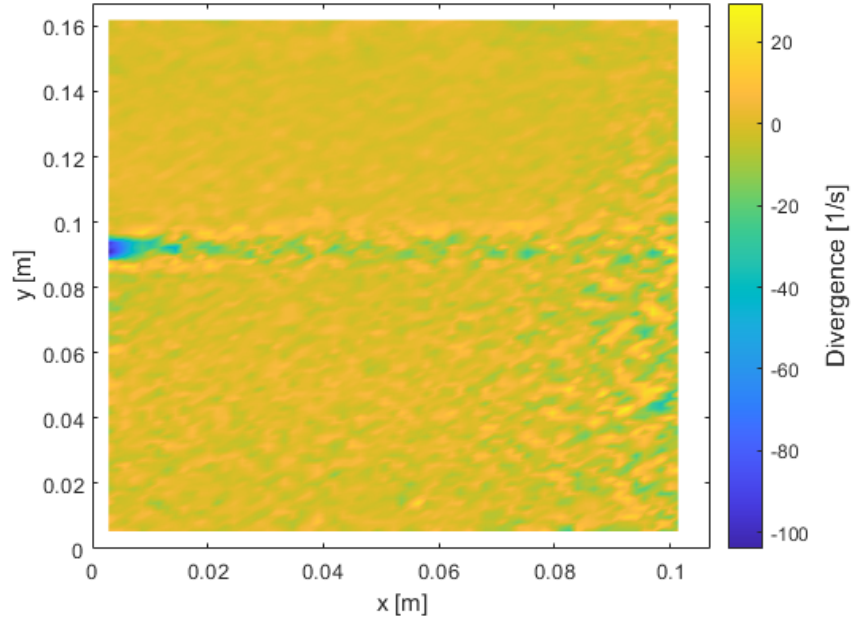


Figure 4.23: Case 2: Divergence field

functions helps reinforce and incorporate the physical principles governing the problem, enabling a more accurate reconstruction of the velocity profile [51].

However, this topic falls outside the main scope of this thesis and will not be further analyzed.

Using the velocity profile from Figure 4.19 and following the steps outlined in section 4.2, it is possible to evaluate the aerodynamic drag and the associated coefficient both for the corrected case and not. The result is presented in Table 4.1.

Case 3: $U_{mean} = 10.6 \text{ m/s} \rightarrow Re \approx 4.5 \cdot 10^4$

The third and final case analysed corresponds to a wind tunnel velocity of $U = 10.6 \text{ m/s}$. Since this case is extremely similar to the previous two measurements, only the essential data needed to compute the drag coefficient of the airfoil under these conditions will be reported, namely, the velocity field and the downstream velocity profile (Figure 4.24 and Figure 4.25).

In this case, the velocity magnitude field appears to be correct and consistent with previous experiments. However, when extracting a velocity profile in the downstream region of the airfoil, some issues can be observed. The free-stream region, which should be characterized by a uniform velocity value that remains constant apart from turbulence intensity, shows an increase in velocity in both

the upper and lower parts. Such a trend has no physical meaning, both because there is no apparent reason for the velocity to behave this way and because the velocity profiles extracted from previous cases also demonstrate the uniformity of the velocity in the free-stream region.

This is a clear indication that the drag coefficient, which will be calculated based on this velocity information, may not be accurate. This aspect will be revisited and explained in more detail in the next section, dedicated to the analysis of the obtained results.

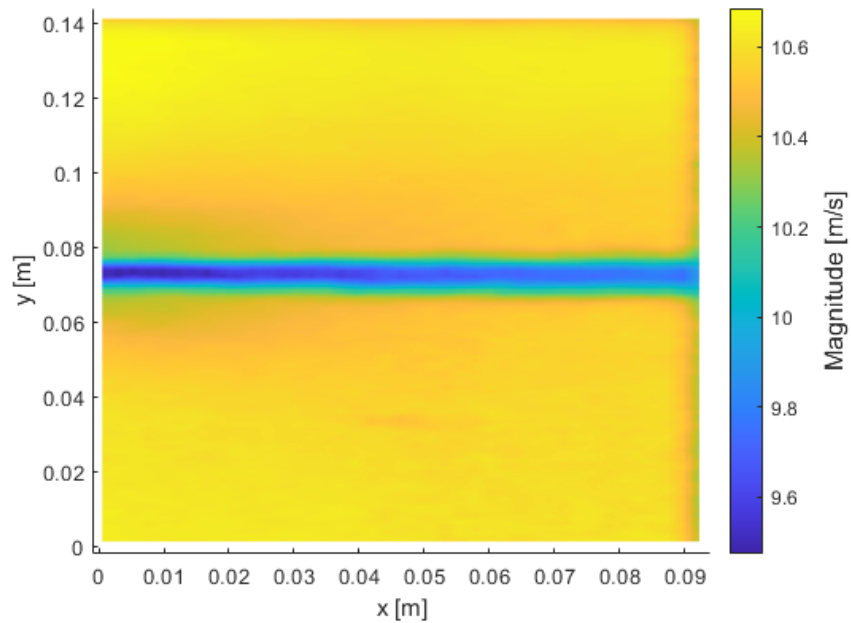


Figure 4.24: Case 3: Magnitude velocity field

4.3.1 Analysis of the results

This section presents the experimental results for calculating the aerodynamic coefficient of a NACA 0012 airfoil at low Reynolds numbers for three different cases in a tabular format.

This was done using Equation 4.5 which, in the absence of plasma (as explained in section 4.2), allows for obtaining the drag (D) generated by the airfoil. From this, the drag coefficient (C_D) can be retrieved simply using the formula:

$$C_D = \frac{2 \cdot D}{\rho U_{in}^2 c} \quad (4.15)$$

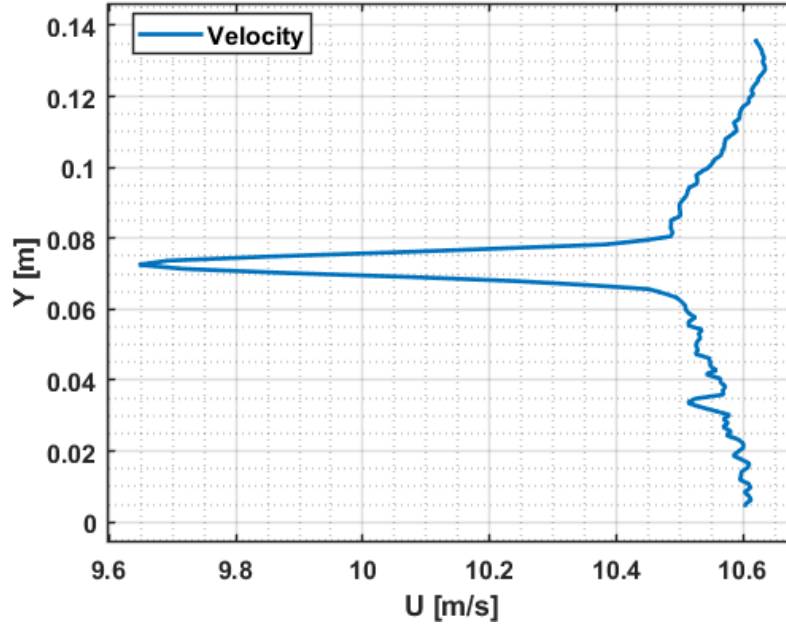


Figure 4.25: Case 3: Downstream velocity profile

where ρ represents the density of air, c is the chord of the airfoil, and U_{in} is the average of the inlet free stream velocity.

As previously specified, both the drag coefficient obtained without accounting for the blockage effect caused by the airfoil inside the wind tunnel ($C_{D_{nc}}$) and the corrected drag coefficient (C_{D_c}) have been reported.

Additionally, to enable a comparison and, more importantly, to validate the obtained values, the same table includes data from two different literature sources referring to the same physical conditions, namely same Reynolds number for a zero angle of attack.

Table 4.1: Drag coefficient for the three cases

	Experimental		Literature	
	$C_{D_{nc}}$	C_{D_c}	<i>Ohtake et al.</i> [52]	<i>Strom et al.</i> [53]
Case 1: $Re \approx 1.0 \cdot 10^4$	0.0434	0.0426	$0.038 < C_D < 0.048$	$0.039 < C_D < 0.043$
Case 2: $Re \approx 2.5 \cdot 10^4$	0.0304	0.0299	$0.026 < C_D < 0.029$	$0.027 < C_D < 0.031$
Case 3: $Re \approx 4.5 \cdot 10^4$	0.0425	0.0419	$0.020 < C_D < 0.025$	$0.022 < C_D < 0.025$

From Table 4.1, the most important aspect that can be observed and pointed out is that two of the three analyzed cases provide results consistent with those obtained by *Ohtake* [52] and *Strom* [53]. Specifically, the first case aligns with both studies found in the literature, while the second is in agreement only with the research conducted by *Strom*.

On the other hand, the third analysis produced a result that is completely off-scale compared to the two previous studies found in the literature. Several factors could explain this discrepancy, but two seem the most probable.

The first concerns the way the PIV technique was performed. The Figure 4.25 clearly shows the presence of a wake near the airfoil. However, in the free-stream region, which should not be influenced by the airfoil, the velocity profile does not remain constant along the y-axis; instead, it tends to increase without ever reaching a uniform trend. This could indicate that the measurement technique was not correctly executed and that, despite achieving a high VDP (as in the previous two experimental cases), the obtained results may not be entirely accurate or representative of the actual conditions happening within the test section.

A second possible reason could be the uncertainty associated with PIV measurements. In this study, no quantification of PIV uncertainty was performed regarding the obtained results, as this remains an open and complex research field where defining a universal uncertainty model is challenging. Therefore, it is possible that the final result is not entirely incorrect but, if the associated uncertainties were considered, it might fall within the range of values calculated in the two previous studies carried out by *Ohtake* and *Strom*.

Furthermore, another aspect worth mentioning is the trend of the drag coefficient developed by the airfoil as the Reynolds number increases. In fact, it tends to decrease as the flow velocity in the test section increases, which is also supported by the two studies found in the literature.

Finally, the last feature that is important to note concerns the correction factor applied to account for the blockage caused by the airfoil inside the test section. At least in this case, it does not seem to play a significant role in the drag coefficient calculation, as the error made by neglecting it is approximately 1.8 %.

This is mainly due to the dimensions of the airfoil relative to those of the test section: with a maximum thickness of 2 mm and a span of about 20 cm, the ratio between the cross-section of the airfoil and the area of the test section is:

$$\frac{A_{airfoil}}{A_{TestSection}} = \frac{0.4 \text{ cm} \cdot 20 \text{ cm}}{20 \text{ cm} \cdot 20 \text{ cm}} \cdot 100 = 2 \%$$

This value is much smaller than the commonly accepted limit in the literature for the maximum blockage ratio, which is around 10 %, to obtain reliable results.

Chapter 5

Conclusions and perspectives

This final chapter aims to analyse the work carried out through a critical assessment to understand the study's strengths and weaknesses. It ultimately draws conclusions regarding the results obtained and the methodology used to achieve them.

Initially, an introductory description (physical concept and state-of-the-art ionic thruster) was developed concerning the new electric propulsion model that the European IPROP project, along with the Von Karman Institute, is advancing. In the same chapter, the main objectives of this thesis were highlighted: the characterization of the flow inside the wind tunnel and the calculation of the drag produced by an airfoil using the optical PIV technique.

Subsequently, the experimental setup used to perform the required measurements was described, accompanied by an in-depth study of four different humidity sensors, which were later employed to create a feedback control loop with the humidifier.

The third chapter focused on the characterization of the flow itself in terms of velocity, temperature, and humidity. Finally, the fourth chapter describes the parametric study conducted for the implementation of the PIV technique and presents the results obtained from the various experimental campaigns, along with their analysis.

As previously specified, the inlet characterization of the test section was the first objective to be completed. In terms of velocity and turbulence, the flow appears to be fairly uniform (Figure 3.1 and Figure 3.2), with a maximum variation of 1 % for velocity and approximately 30 % for turbulence intensity. Despite this, the turbulence intensity remains at very low levels, consistent with what is expected from a properly constructed wind tunnel. This variation may be due to the fact that turbulence intensity was calculated using a Pitot tube, an instrument not

particularly suitable for this type of application. The use of hot-wire anemometry would be more appropriate and would allow for a more accurate evaluation of this parameter.

Regarding temperature, it was shown that in the absence of internal resistance, the flow exhibits a uniform distribution. However, when the heater is activated, the airflow loses its homogeneity. Consequently, strategies should be adopted to improve this feature so that, in the future, the effect of temperature on the thruster can be studied more consistently and accurately.

Another observation concerns the high-velocity test cases (Figure 3.6 and Figure 3.8): the airflow passing through the lower part of the test section is characterized by a significantly lower temperature compared to the upper part. This suggests the potential use of a heater with a higher maximum power than the one currently employed, in order to achieve a wider temperature range and improve uniformity.

The same considerations made for temperature also apply to humidity. In the absence of vapor injection into the wind tunnel, the uniformity level within the test section is very high, with a maximum variation of less than one percent (Figure 3.9). However, when the humidifier is activated, this homogeneity is lost, and a significant humidity gradient develops between the upper and lower parts of the test section (Figure 3.10). This issue has been partially addressed by adding two steam sprayers inside the wind tunnel to cover a larger area. Nonetheless, additional mixing strategies should be implemented to further improve the uniformity of the flow.

At the same time, the objective of achieving a constant and controlled humidity flow was partially met through a feedback control loop developed using the humidifier and the P14 humidity sensor—the last one analyzed, which provided the best performance in terms of response and recovery time.

In the future, further improvements should be made to make this control more stable and accurate, allowing for the most precise possible testing of the effect of humidity on the ionic air-breathing thruster.

The second objective of this thesis focused on using the optical Particle Image Velocimetry (PIV) technique to calculate the drag and its corresponding coefficient for a well-known airfoil, the NACA0012, placed inside the test section to simulate the ionic thruster prototype that will be used in the future. As previously stated, knowing the drag produced by the obstacle is crucial for determining the total effective thrust generated by the propulsion system once the ionization mechanism is activated. Consequently, it was necessary to develop an appropriate methodology for calculating this parameter.

In general, the results obtained are consistent with those found in the literature, demonstrating the validity of the PIV technique in this context for estimating the drag produced by the airfoil and the test section itself. However, in some cases (such as the third entry in Table 4.1), the methodology used can yield entirely

incorrect results, falling outside the predicted ranges from previous studies. In most instances, this can be attributed to an improper execution of the optical technique. However, during the various tests conducted, it was observed that the method described in section 4.2 is also highly dependent on external variables such as the flow temperature and the measured pressure values.

In particular, measuring the airflow temperature inside the test section is essential for accurately determining the air density. This latter plays a critical role in calculating the drag generated by the airfoil, and it was observed that even a small temperature variation can significantly alter the results. Therefore, a more precise and reliable temperature measurement is fundamental to ensuring accurate outcomes.

The same reasoning applies to the calculation of the pressure variation between the inlet and outlet of the control volume. In this study, due to the lack of pressure tabs in the upstream region of the airfoil, Bernoulli's principle was exploited, assuming that total pressure remains constant in an incompressible flow. However, this principle is only applicable in scenarios where frictional effects due to flow viscosity are absent or negligible. Since viscosity is one of the key factors contributing to the drag generated by the airfoil, the application of this method in this context is not highly precise.

Therefore, in future measurements, greater attention should be given to accurately determining the pressure drop between the inlet and outlet of the airfoil. The use of pressure taps upstream and downstream of the profile is recommended. However, in their absence, considering that the flow under study is incompressible, the use of penalized and constrained Radial Basis Functions would allow for computing an analytical representation of velocity and pressure fields [51].

All this leads to the conclusion that, during future experimental campaigns, before proceeding with the calculation of the actual thrust developed by the thruster, it will be necessary to conduct an accurate and precise measurement of the drag generated by the thruster itself and verify that the results are consistent with those obtained in this thesis and, more generally, with the literature.

One final aspect worth mentioning concerns the blockage correction factor, discussed in previous sections. As previously stated, since the airfoil used in this study is relatively small compared to the test section, the blockage effect was practically negligible. However, the future development of this project aims to study the thruster with not just one but four airfoil stacked on top of each other inside the test section. In this scenario, the transverse dimensions of the airfoil will be comparable to those of the test section, making the blockage factor significant and no longer negligible.

In conclusion, this thesis is only the starting point of a larger project: further experimental testing must be carried out to really get to know how the performances of the thruster are affected by external environmental conditions.

Bibliography

- [1] Belan M. Kahol O. et al. «Scaling relations for the geometry of wire-to-airfoil atmospheric ionic thrusters». In: *Journal of Electrostatics* 123 (Dec. 2022) (cit. on pp. 1, 2, 6, 52).
- [2] European Parliament and European Union Council. *REGULATION (EU) 2023/2405 of 18 October 2023 on ensuring a level playing field for sustainable air transport (ReFuelEU Aviation)*. <https://eur-lex.europa.eu/legal-content/EN/TXT/PDF/?uri=CELEX:32023R2405>. 2014 (cit. on p. 1).
- [3] Wenping Cao, Barrie C. Mecrow, Glynn J. Atkinson, John W. Bennett, and David J. Atkinson. «Overview of Electric Motor Technologies Used for More Electric Aircraft (MEA)». In: *IEEE Transactions on Industrial Electronics* 59 (2012) (cit. on p. 1).
- [4] Benjamin J. Brelje and Joaquim R.R.A. Martins. «Electric, hybrid, and turboelectric fixed-wing aircraft: A review of concepts, models, and design approaches». In: *Progress in Aerospace Sciences* 104 (2019) (cit. on p. 1).
- [5] Barrett S. R. H. Masuyama K. «On the performance of electrohydrodynamic propulsion». In: *Proc. R Soc A* 469 (Mar. 2013) (cit. on pp. 2, 4, 5, 52).
- [6] Leishman J. G. *Principles of Helicopter Aerodynamics*. Cambridge: Cambridge Univ. Press, 2000 (cit. on p. 2).
- [7] Barrett S. R. H. Xu H. He Y. et al. «Flight of an aeroplane with solid-state propulsion». In: *Nature* 563 (Nov. 2018) (cit. on pp. 2, 3, 5).
- [8] Nicolas Monrolin, Franck Plouraboué, and Olivier Praud. «Electrohydrodynamic Thrust for In-Atmosphere Propulsion». In: *AIAA Journal* 55 (Sept. 2017) (cit. on pp. 3, 5, 52).
- [9] Tong Lin, Mingying Huo, Naiming Qi, Jianfeng Wang, Tianchen Wang, Haopeng Gu, and Yiming Zhang. «Coupling Dynamics and Three-Dimensional Trajectory Optimization of an Unmanned Aerial Vehicle Propelled by Electroaerodynamic Thrusters». In: *Aerospace* 10 (Nov. 2023), p. 950 (cit. on pp. 3, 6).

- [10] Jack Wilson, H. Douglas Perkins, and William K. Thompson. «An Investigation of Ionic Wind Propulsion». In: *NASA/TM-2009-215822* (2009) (cit. on pp. 3, 52).
- [11] Brown T. T. «A method of an Apparatus or Machine for Producing Force and Motion». In: *G.B. Patent 300311* (1928) (cit. on p. 4).
- [12] Brown T. T. «Electrokinetic Apparatus». In: *U.S. Patent 2,949,550* (Aug. 1960) (cit. on p. 4).
- [13] Christenson E. and Moller P. «Ion-neutral propulsion in atmospheric media». In: *AIAA Journal* 5 (Oct. 1967) (cit. on p. 4).
- [14] George Matsoukas and N.A. Ahmed. «Experimental Investigation of Employing Asymmetrical Electrodes in Propulsion of Vehicles». In: *Procedia Engineering* 49 (Dec. 2012), pp. 247–253 (cit. on pp. 4, 52).
- [15] Vladislav Yu. Khomich and Igor E. Rebrov. «In-atmosphere electrohydrodynamic propulsion aircraft with wireless supply onboard». In: *Journal of Electrostatics* 95 (2018), pp. 1–12 (cit. on p. 5).
- [16] L. Zhao and K. Adamiak. «EHD gas flow in electrostatic levitation unit». In: *Journal of Electrostatics* 64.7 (2006) (cit. on p. 5).
- [17] Alexandre A. Martins and Mario J. Pinheiro. «Modeling of an EHD corona flow in nitrogen gas using an asymmetric capacitor for propulsion». In: *Journal of Electrostatics* 69.2 (2011), pp. 133–138 (cit. on p. 5).
- [18] Belan M. et al. «A parametric study of electrodes geometries for atmospheric electrohydrodynamic propulsion». In: *Journal of Electrostatics* 113 (July 2021) (cit. on pp. 5, 53).
- [19] Belan M. et al. «Effects of the emitters density on the performance of an atmospheric ionic thruster». In: *Journal of Electrostatics* 120 (Oct. 2022) (cit. on pp. 6, 53, 56).
- [20] Nicolas Balcon Eric Moreau Nicolas Benard. «Electric Wind Produced by a Surface Dielectric Barrier Discharge Operating Over a Wide Range of Relative Humidity». In: *47th AIAA Aerospace Sciences Meeting, AIAA Paper* (2012) (cit. on p. 7).
- [21] David Ashpis and Matthew Laun. «Dielectric Barrier Discharge Plasma Actuator Thrust Measurement Methodology Incorporating Antithrust Hypothesis». In: *AIAA Journal* 55 (Sept. 2017), pp. 1–12. DOI: 10.2514/1.J055856 (cit. on p. 7).
- [22] Michael Wicks and Flint O. Thomas. «Effect of Relative Humidity on Dielectric Barrier Discharge Plasma Actuator Body Force». In: *AIAA Journal* (July 2015). DOI: 10.2514/1.J055856 (cit. on p. 7).

- [23] W. Kim; H. Do; M. G. Mungal; M. A. Cappelli. «On the role of oxygen in dielectric barrier discharge actuation of aerodynamic flows». In: *Applied physics* (Oct. 2007) (cit. on p. 8).
- [24] Takehiko Segawa, Hirohide Furutani, Hiro Yoshida, Timothy Jukes, and Kwing-So Choi. «Wall Normal Jet under Elevated Temperatures Produced by Surface Plasma Actuator». In: Jan. 2007. ISBN: 978-1-62410-012-3. DOI: 10.2514/6.2007-784 (cit. on p. 8).
- [25] Douglas R Neal Dirk Michaelis and Bernhard Wieneke. «Impact of Pressure and Temperature on the Performance of Plasma Actuators». In: *Measurements Science and Technology* 27 (Sept. 2016). DOI: 10.2514/1.43852 (cit. on p. 8).
- [26] The European Innovation Council (EIC). *Ionic Propulsion in atmosphere*. 2023. URL: <https://cordis.europa.eu/project/id/101098900/it> (cit. on p. 9).
- [27] Von Kamran Insitute for Fluid Dynamics. *Low speed open-loop wind tunnel L7*. 2019. URL: <https://www.vki.ac.be/index.php/48-research-and-consulting/facilities/low-speed-wind-tunnels/62-low-speed-mini-wind-tunnel-1-7-to-1-13> (cit. on pp. 11, 12).
- [28] Chabih Dris Youssef. «Adaptation d’une soufflerie basse vitesse pour simulation de conditions environnementales (Humidité et Température)». Master Thesis. Institut Supérieur Industriel de Bruxelles, 2022 (cit. on pp. 12, 13).
- [29] *Temperature and humidity sensor*. CAREL (cit. on p. 18).
- [30] *Digital-output relative humidity and temperature sensor/module*. Aosong Electronics Co.,Ltd (cit. on p. 18).
- [31] Testo. *High-precision humidity/temperature probe (digital) - wired*. URL: <https://www.testo.com/en/high-precision-humidity/temperature-probe-digital/p/0636-9772> (cit. on p. 19).
- [32] *P14, Capacitive Humidity Sensor*. Innovative Sensor Technology (IST) (cit. on p. 19).
- [33] Ashis Tripathy, Sumit Pramanik, Jongman Cho, Jayasree Santhosh, and Noor Azuan Abu Osman. «Role of Morphological Structure, Doping, and Coating of Different Materials in the Sensing Characteristics of Humidity Sensors». In: *Sensors (Basel, Switzerland)* 14 (Sept. 2014), pp. 16343–16422. DOI: 10.3390/s140916343 (cit. on p. 22).
- [34] Vaisala. *Technical note: Response time in humidity measurements*. Tech. rep. www.vaisala.com, 2018 (cit. on p. 23).
- [35] M. Hamdi, Michel Havet, • Rouaud, and • Tarlet. «Comparison of different tracers for PIV measurements in EHD airflow». In: 55 (Mar. 2014) (cit. on p. 34).

-
- [36] Mendez and Laboureur. *An Introduction to Particle image Velocimetry (PIV)*. Introduction to measurements techniques. 2024 (cit. on p. 35).
- [37] Sven Scharnowski and Christian J. Kähler. «Particle image velocimetry - Classical operating rules from today's perspective». In: *Optics and Lasers in Engineering* 135 (2020), p. 106185. ISSN: 0143-8166. DOI: <https://doi.org/10.1016/j.optlaseng.2020.106185>. URL: <https://www.sciencedirect.com/science/article/pii/S0143816619318287> (cit. on p. 36).
- [38] Belan M. Trovato S. «Wind tunnel testing and performance modeling of an atmospheric ion thruster». In: *Journal of Physics D: Applied Physics* 58 (Oct. 2024). DOI: 10.1088/1361-6463/ad7d9c (cit. on p. 42).
- [39] K Okamoto, S Nishio, T Saga, and Kobayashi. «Standard images for particle-image velocimetry». In: *Measurement Science and Technology* 11 (May 2000), p. 685. DOI: 10.1088/0957-0233/11/6/311 (cit. on p. 43).
- [40] Adam Fincham and Geoffrey Spedding. «Low cost, high-resolution DPIV for measurement of turbulent fluid flow». In: *Experiments in Fluids* 23 (Dec. 1997), pp. 449–462. DOI: 10.1007/s003480050135 (cit. on p. 43).
- [41] William Thielicke and E J Stamhuis. «PIVlab – Towards User-friendly, Affordable and Accurate Digital Particle Image Velocimetry in MATLAB». In: *Journal of Open Research Software* 2 (Oct. 2014). DOI: 10.5334/jors.bl (cit. on pp. 43, 44).
- [42] William Thielicke and Rene Sonntag. «Particle Image Velocimetry for MATLAB: Accuracy and enhanced algorithms in PIVlab». In: *Journal of Open Research Software* 9 (May 2021). DOI: 10.5334/jors.334 (cit. on pp. 43, 44).
- [43] M.A. Mendez, M. Raiola, A. Masullo, S. Discetti, A. Ianiro, R. Theunissen, and J.-M. Buchlin. «POD-based background removal for particle image velocimetry». In: *Experimental Thermal and Fluid Science* 80 (2017), pp. 181–192. ISSN: 0894-1777. DOI: <https://doi.org/10.1016/j.expthermflusci.2016.08.021>. URL: <https://www.sciencedirect.com/science/article/pii/S0894177716302266> (cit. on p. 43).
- [44] Ravi Sankar Vaddi, Yifei Guan, Alexander Mamishev, and Igor Novosselov. «Analytical model for electrohydrodynamic thrust». In: *Proceedings of The Royal Society A* 476 (Sept. 2020) (cit. on pp. 51, 52).
- [45] Eric Moreau, Nicolas Benard, Jean-Daniel Lan-Sun-Luk, and Jean-Pierre Chabriat. «Electrohydrodynamic force produced by a wire-to-cylinder dc corona discharge in air at atmospheric pressure». In: *Journal of Physics D: Applied Physics* 46.47 (Oct. 2013), p. 475204 (cit. on p. 52).

- [46] M.R. Homaeinezhad and M. Nesaeeian. «Analytical model for corona discharge-based electrohydrodynamic plasma actuator incorporating environmental conditions». In: *Acta Astronautica* 210 (2023), pp. 224–236 (cit. on p. 53).
- [47] Seung-Hee Kang, Eui Shin, Ki-Wahn Ryu, and Jun-shin Lee. «Separation blockage-correction method for the airfoil of a wind turbine blade». In: *Journal of Mechanical Science and Technology* 27 (May 2013). DOI: 10.1007/s12206-012-1261-2 (cit. on p. 59).
- [48] Glenn Brown. «The History of the Darcy-Weisbach Equation for Pipe Flow Resistance». In: *Proc. Environ. Water Resour. Hist.* 38 (Oct. 2002). DOI: 10.1061/40650(2003)4 (cit. on p. 59).
- [49] Christian J. Kähler Sven Scharnowski A. Sciacchitano. «A new look on the “Valid Detection Probability” of PIV Vectors». In: *Research Group Aerodynamics (TU Delft)* (2018) (cit. on p. 61).
- [50] Philippe Versailles, Vincent Gingras-Gosselin, and Huu Vo. «Peak-locking reduction for particle image velocimetry». In: *AIAA J.* 48 (Apr. 2010), pp. 859–863. DOI: 10.1088/0957-0233/27/10/104005 (cit. on p. 66).
- [51] Pietro Sperotto, Manuel Ratz, and Miguel Mendez. «SPICY: a Python toolbox for meshless assimilation from image velocimetry using radial basis functions». In: (July 2023) (cit. on pp. 74, 80).
- [52] Tomohisa Ohtake, Yusuke Nakae, and Tatsuo Motohashi. «Nonlinearity of the Aerodynamic Characteristics of NACA0012 Aerofoil at Low Reynolds Numbers». In: *Journal of The Japan Society for Aeronautical and Space Sciences* 55 (Oct. 2007), pp. 439–445. DOI: 10.2322/jjsass.55.439 (cit. on pp. 76, 77).
- [53] Benjamin Strom, Noah Johnson, and Brian Polagye. «Impact of blade mounting structures on cross-flow turbine performance». In: *Journal of Renewable and Sustainable Energy* 10 (May 2018), p. 034504. DOI: 10.1063/1.5025322 (cit. on pp. 76, 77).